

# The Luminosity Function of Star Clusters in Spiral Galaxies <sup>1</sup>

Søren S. Larsen <sup>2</sup>

*UC Observatories / Lick Observatory, University of California, Santa Cruz, CA 95064, USA*

soeren@ucolick.org

## ABSTRACT

Star clusters in 6 nearby spiral galaxies are examined using archive images from the Wide Field Planetary Camera 2 (WFPC2) on board the Hubble Space Telescope (HST). The galaxies have previously been studied from the ground and some of them are known to possess rich populations of “young massive clusters” (YMCs). Comparison with the HST images indicates a success-rate of  $\sim 75\%$  for the ground-based cluster detections, with typical contaminants being blends or loose groupings of several stars in crowded regions. The luminosity functions (LFs) of cluster candidates identified on the HST images are analyzed and compared with existing data for the Milky Way and the LMC. The LFs are well approximated by power-laws of the form  $dN(L)/dL \propto L^\alpha$ , with slopes in the range  $-2.4 \lesssim \alpha \lesssim -2.0$ . The steeper slopes tend to be found among fits covering brighter magnitude intervals, although direct hints of a variation in the LF slope with magnitude are seen only at low significance in two galaxies. The surface density of star clusters at a reference magnitude of  $M_V = -8$ ,  $\Sigma_{\text{cl}}^{-8}$ , scales with the mean star formation rate per unit area,  $\Sigma_{\text{SFR}}$ . Assuming that the LF can be generally expressed as  $dN(L)/dL = c A \Sigma_{\text{SFR}}^\gamma L^\alpha$ , where  $A$  is the galaxy area,  $\gamma \sim 1.0 - 1.4$ ,  $\alpha = -2.4$  and the normalization constant  $c$  is determined from the WFPC2 data analyzed here, the maximum cluster luminosity expected in a galaxy from random sampling of the LF is estimated as a function of  $\Sigma_{\text{SFR}}$  and  $A$ . The predictions agree well with existing observations of galaxies spanning a wide range of  $\Sigma_{\text{SFR}}$  values, suggesting that sampling statistics play an important role in determining the maximum observed luminosities of young star clusters in galaxies.

*Subject headings:* galaxies: star clusters — galaxies: spiral — galaxies: individual (NGC 628, NGC 1313, NGC 3184, NGC 5236, NGC 6744, NGC 6946)

---

<sup>1</sup>Based on observations obtained with the NASA/ESA Hubble Space Telescope, obtained at the Space Telescope Science Institute, which is operated by the Association of Universities for Research in Astronomy, Inc. under NASA contract No. NAS5-26555.

<sup>2</sup>Guest User, Canadian Astronomy Data Centre, which is operated by the Herzberg Institute of Astrophysics, National Research Council of Canada

## 1. Introduction

Since the launch of the Hubble Space Telescope (HST), the ubiquity of highly luminous young star clusters in starburst environments, sometimes referred to as “super star clusters” (SSCs), has been firmly established. Some of the best-known cases include merger galaxies such as the “Antennae” (Whitmore & Schweizer 1995) and NGC 3256 (Zepf et al. 1999), but SSCs have also been found in galaxies that do *not* show any obvious indications of having been involved in recent merger events. Examples of isolated starburst dwarfs with SSCs are NGC 1569 and NGC 1705 (Arp & Sandage 1985; O’Connell et al. 1994). The Large Magellanic Cloud also contains a number of “blue populous” or “young massive” clusters (YMCs) (Shapley & Nail 1951; Hodge 1961), many of which have ages characteristic of Milky Way *open* clusters, i.e. a few times  $10^8$  years or younger, but are an order of magnitude more massive than any young cluster that is known in our Galaxy today. Such clusters are also present in some spiral galaxies, and there appears to be a fairly tight relation between the star formation rates (SFRs) of galaxies and the number of YMCs (Larsen and Richtler 2000, hereafter LR2000).

The current terminology is confusing and reflects, to a large extent, a lack of understanding of how different types of clusters are related. The terms “populous”, “massive” and “super” clusters were introduced as a reference to star clusters that apparently have no counterpart in our Galaxy, but do they actually constitute a separate class of objects, fundamentally different from low-mass “open” clusters? Do they require special conditions to form? There is not really any *a priori* reason to assume that the open cluster system in the Milky Way is representative for other galaxies or even other spirals, and by the same token, the *presence* of YMCs in e.g. the LMC may be no more unusual than their *absence* in our Galaxy. It may be more appropriate to view the cluster system of our Galaxy as part of a continuum that ranges from very cluster-poor galaxies with low SFRs such as IC 1613 (Wyder, Hodge, & Cole 2000), over our Galaxy, to the LMC and finally to starburst environments.

Simple statistics may play a role in determining the luminosity of the brightest cluster in a galaxy, since random sampling of a power-law luminosity function (LF) will give brighter clusters in galaxies with richer cluster systems (Whitmore 2001). Rich cluster systems, in turn, would generally be expected in galaxies with high levels of star formation. In addition to statistical effects there may be a physical upper limit to the mass of star clusters that can form in a galaxy, determined by factors such as the gas density and -pressure of the interstellar medium which are also expected to correlate with the overall star formation rate (Elmegreen & Efremov 1997; Kennicutt 1998; Billett, Hunter & Elmegreen 2002). It is currently unclear to what extent sampling statistics or physics dominate the maximum observed cluster luminosities and -masses, and under what conditions one or the other might prevail.

In reality, very little is known about how the LF of young cluster populations depends on environment. van den Bergh & Lafontaine (1984) found that the LF of Milky Way open clusters is well described as a power-law of the form  $dN(L)/dL \propto L^\alpha$  with  $\alpha = -1.5$  for  $-8 < M_V < -2$ , but

may steepen somewhere in the range  $-11 < M_V < -8$ . Studies of young cluster populations in other galaxies generally find somewhat steeper slopes,  $-2.5 \lesssim \alpha \lesssim -2.0$  (e.g. Dolphin & Kennicutt 2002; Zepf et al. 1999), and Whitmore et al. (1999) suggested a bend at  $M_V \sim -10.4$  for young clusters in the Antennae with  $\alpha = -2.6 \pm 0.2$  for brighter clusters and  $\alpha = -1.7 \pm 0.2$  for fainter clusters. Unfortunately, there is little overlap between observations of open clusters in the Milky Way, which cover a very limited section of our Galaxy and include few clusters *brighter* than  $M_V \approx -9$ , and studies of young clusters in external galaxies where the identification of clusters *fainter* than  $M_V \approx -8$  is difficult because of the risk of confusion with individual, luminous stars. Even with HST, unambiguous identification of star clusters in crowded environments is problematic at distances greater than 10–15 Mpc.

Considering the diversity of properties encountered among young cluster populations even in normal spirals, HST images of nearby spirals may provide some insight into correlations between properties of the cluster systems and host galaxy parameters. The HST archive contains a number of WFPC2 datasets covering nearby spiral galaxies, including many of those studied by LR2000. At the typical distances of these galaxies ( $\approx 5$  Mpc), one WF pixel corresponds to a linear scale of 2–3 pc, comparable to the typical half-light radius of a star cluster. This makes it possible to identify star clusters based on their angular extent and thereby greatly reduce the risk of contamination by individual stars. In this paper I examine HST archive images of 6 selected galaxies from LR2000, some of which possess rich populations of YMCs while others have more modest, presumably more Milky Way-like cluster populations. As with any survey based on archive data, the choices of exposure times, filters and exact pointing are limited by what happens to be available. However, even with exposures in only one band one can perform interesting comparisons of the cluster populations in different galaxies. As a bonus, the WFPC2 data can be used for a check of the ground-based cluster identifications. The detailed structure of individual clusters will be investigated in a forthcoming paper.

## 2. Data

The data were downloaded from the HST archive at the Canadian Astronomy Data Centre (CADC) with standard “on-the-fly” pipeline processing. Only datasets including exposures longer than about 5 min in a  $V$ -band equivalent (F547M, F555W or F606W) were considered. When several exposures in a band were available they were combined using the CRREJ task in the STSDAS package in IRAF<sup>3</sup> to eliminate cosmic ray hits. The WFPC2 datasets used in this paper are listed in Table 1 and the pointings are shown in Fig. 1. As seen in Fig. 1, the pointings cover different parts of the respective galaxies relative to the center, spiral arms etc, and a more uniform coverage would certainly have been important in a dedicated survey. Nevertheless, the archive data

---

<sup>3</sup>IRAF is distributed by the National Optical Astronomical Observatories, which are operated by the Association of Universities for Research in Astronomy, Inc. under contract with the National Science Foundation

used here should still provide a basis for a first rough intercomparison of star clusters in the different galaxies. In some cases the PC chip is centered on the galaxy nucleus but the main focus in this paper is on clusters in the disks, and the nuclear regions, where crowding and dust extinction may pose more serious problems, have generally been avoided.

Objects were detected using the DAOFIND task in DAOPHOT (Stetson 1987) running within IRAF, using a  $3\sigma$  detection threshold. When exposures in more than one band were available, DAOFIND was run independently on each exposure and the resulting object lists were matched to reduce the number of spurious detections. Aperture photometry was then done with the APPHOT task in DAOPHOT, using aperture radii of 3 and 5 pixels. When only one band was available, calibration of the photometry to standard  $V$  magnitudes was provided by the zero-points in the *WFPC2 handbook*<sup>4</sup>. Otherwise the transformations in Holtzman et al. (1995) were used. Aperture corrections were determined by convolving a synthetic point spread function (PSF) generated by TinyTim (Krist and Hook 1997) with various models for the cluster profiles and measuring the flux within apertures of various sizes. The results are listed in Table 2 for aperture radii of 3 and 20 pixels, relative to a reference aperture of 5 pixels (Holtzman et al. 1995). In addition to point sources (the pure TinyTim PSF), the aperture corrections were determined for King and Moffat models (Larsen 1999b) with FWHM of 0.5 and 1.0 pixels, covering the typical range of intrinsic cluster sizes expected in the galaxies. The calibration by Holtzman et al. (1995) includes an implicit correction of 0.1 mag from their  $0''.5$  reference aperture to infinity, which agrees fairly well with the aperture correction from  $r = 5$  to  $r = 20$  pixels for point sources in Table 2. However, magnitudes measured in the  $r = 5$  pixels aperture will be underestimated by an additional  $\sim 0.1$  mag for the most extended objects. For an aperture radius of 3 pixels, the magnitudes of objects with FWHM=0.5 and 1.0 pixels will be too faint by about 0.12 mag and 0.35 mag, respectively (assuming King  $c = 30$  profiles), if the  $-0.06$  mag aperture corrections for point sources are used. For accurate integrated photometry of the clusters, knowledge of their intrinsic light profiles would be needed, but for the present purpose it was decided to simply use an aperture correction of  $-0.30$  mag for photometry in the  $r = 3$  pixels aperture. Finally, note that the size-dependent corrections for *colors* are generally negligible.

Sizes were measured for all objects using the `ishape` code. The code is described in detail in Larsen (1999b), and extensive tests of its performance have been carried out in that paper and elsewhere (e.g. Larsen, Forbes & Brodie 2001). Briefly, intrinsic object sizes are measured by adopting an analytic model of the source and convolving the model with the PSF, adjusting the shape parameters (FWHM, orientation, ellipticity) until the best match to the observed image is obtained. For the analytic model a King  $c = 30$  profile was used, while the PSF was modeled with TinyTim. When exposures of adequate depth were available in several bands, the sizes were obtained as an average of measurements in each band.

Distances to the galaxies were taken from the references in Larsen and Richtler (1999), except

---

<sup>4</sup>available at the URL <http://www.stsci.edu/instruments/wfpc2>

for NGC 6946 where a distance modulus of 28.9 was assumed (Karachentsev, Sharina & Huchmeier 2000). Corrections for Galactic foreground extinction were applied according to Schlegel et al. (1998) as provided by the *NASA/IPAC Extragalactic Database* (NED). The adopted distance moduli and reddenings are listed in Table 1. Even though the galaxies studied here are oriented nearly face-on so that the effect of internal extinction is minimized, significant extinction may still be present in some areas, especially within dusty regions in spiral arms where  $A_B$  can exceed 1 mag (e.g. Keel & White 2001a; Keel and White 2001b). In Sect 4.2, *UBV* data are used to obtain reddening estimates for clusters in one of the fields, suggesting modest reddenings for most of those clusters ( $A_V \lesssim 1$  mag). In the other fields there is no information available about the reddenings of individual clusters, so reddening within the galaxies has generally been ignored. Some considerations concerning the effect of variable extinction on the observed luminosity functions are given in Sect 5.4.

### 3. Comparison of ground-based and WFPC2 data for clusters in NGC 6946

Because of the complete *UBVI* coverage the data from HST Program 8715 (field NGC 6946–3) are very suitable for a comparison with the ground-based data used in LR2000. WFPC2 images of all cluster candidates in this field identified from the ground are shown in Fig. 2 with each panel covering a  $40 \times 40$  pixels ( $4'' \times 4''$ ) section around each candidate. An extremely luminous cluster contained within the PC chip is discussed elsewhere (Larsen et al. 2001a) and has been omitted here. Ground-based and WFPC2 *UBVI* photometry and sizes are listed in Table 3. Most of the objects in Fig. 2 are clearly extended and very likely clusters. With adequate S/N, objects with intrinsic FWHM down to 0.2 pixels can be resolved by *ishape* (e.g. Larsen, Forbes & Brodie 2001), corresponding to about 0.8 pc at the assumed distance of NGC 6946. Only one object (#2350) is smaller than this limit, but this object is far too bright to be an individual star ( $M_V = -10.8$ , from the WFPC2 data) and is most likely a very compact cluster. For objects #1490, #2210 and #2745 the classification as star clusters is more dubious, because these are located in crowded areas where a blend of two or more stars might be mistaken by *ishape* for a cluster. For this reason, these three objects have been omitted from Table 3. It therefore appears that about 3 of the 13 objects in Fig. 2 might be non-clusters, indicating a “contamination” fraction for the ground-based cluster identifications of  $\approx 25\%$ . Inspection of ground-selected cluster candidates on the full set of WFPC2 images in Table 1 corroborates this estimate and a similar conclusion was reached for a ground-based survey of young clusters in M51 (Larsen 2000).

The WFPC2 photometry in Table 3 was done with an  $r = 5$  pixels aperture, correcting the *V* magnitudes by  $-0.1$  mag to account for the extended nature of the objects. Even after that correction, the ground-based *V* magnitudes remain somewhat brighter than those measured on the WFPC2 images, with a mean difference of  $\langle V_{\text{ground}} - V_{\text{HST}} \rangle = -0.37$  mag. For *colors* the systematic differences are very small, with  $\langle (U-B)_{\text{ground}} - (U-B)_{\text{HST}} \rangle = 0.01$ ,  $\langle (B-V)_{\text{ground}} - (B-V)_{\text{HST}} \rangle = -0.03$  and  $\langle (V-I)_{\text{ground}} - (V-I)_{\text{HST}} \rangle = -0.02$ . The offset in *V* magnitude is most

likely due to the use of a much larger aperture ( $1''.5$ ) for the ground-based measurements, including contributions from nearby stars and clusters which do not fall within the smaller aperture used for the WFPC2 photometry. To test if this can account for the difference between HST and ground-based photometry,  $V$  magnitudes for the clusters were also measured in an  $r = 15$  pixels ( $1''.5$ ) aperture on the HST images. These are listed in Table 3 as  $V_{15}$ , except for object #1371 which is too close to the edge of the WF4 chip. The measurements in this larger aperture do indeed agree very well with the ground-based ones, with a mean difference of only  $\langle V_{\text{ground}} - V_{15,\text{HST}} \rangle = -0.007$  mag.

Concerning the sizes, it is clear that huge differences exist between the measurements on ground-based and WFPC2 images. Again, this can be attributed to the presence of other objects near the cluster candidates, which tend to blur the ground-based images and make the clusters look bigger than they are. This has been discussed in detail in Larsen (1999a), where it was also shown that even relatively distant “neighbors” can affect the size estimates significantly.

## 4. Properties of Young Clusters in the WFPC2 fields

### 4.1. Selection of cluster candidates

Even relatively short WFPC2 exposures allow cluster candidates to be identified with reasonable confidence to much fainter limiting magnitudes than from the ground because of the better angular resolution and improved contrast. Reliable size measurements require a S/N of 30–50 (Larsen 1999b), which is reached in about 10 min with the F555W filter for a  $V = 23$  object superimposed on a moderately bright sky background, such as that encountered within the disk of a spiral galaxy. With the same exposure time, the broader F606W filter permits size measurements for somewhat fainter objects.

Fig. 3 shows the intrinsic FWHM values as a function of  $V$  magnitudes for all objects in the NGC 6946–3 field. In this figure and throughout the rest of this paper, all photometry was done in an  $r = 3$  pixels aperture. For objects brighter than  $V \sim 23$ , there is a fairly clear separation between extended sources and compact, unresolved objects which fall near the  $x$ -axis and have  $\text{FWHM} \lesssim 0.1$  pixel. To reduce the risk of including contaminants in the cluster lists, relatively conservative size- and magnitude limits were chosen. For the data in Fig. 3, cluster candidates were selected as objects with  $V < 22.5$  and  $\text{FWHM} > 0.2$  pixels. For the other fields the adopted magnitude cuts ranged between  $V = 22$  and  $V = 23$ , depending on the quality of the data. To ensure homogeneity in the selection of cluster candidates, no other selection criteria, such as color cuts, were applied since some datasets contained exposures in only one band.

The magnitude cuts used for selection of the cluster samples are well above the level where completeness effects are important. This is illustrated in Fig. 4, which shows completeness functions for each WFPC2 field. The completeness functions were determined by adding artificial sources

to each of the WF chips at random positions (but with minimum separations of 10 pixels) and redoing the detection- and photometry procedures and counting how many of the artificial sources that were recovered. Objects with magnitudes between  $V = 20$  and  $V = 25$  were added at 0.5 mag intervals, with 500 objects per chip at each magnitude step. The artificial objects were modeled as King profiles with an intrinsic FWHM of 0.5 pixels, convolved with the `TinyTim` point-spread function. Note that the completeness is not a simple function of the exposure times (see Table 1), but depends on factors such as the sky background in the individual fields, degree of crowding etc. The solid parts of the curves in Fig. 4 represent the magnitude intervals used for luminosity function analysis in Sec 4.3. In all cases the completeness is formally better than 93% in the relevant magnitude intervals. It should, however, be stressed that these tests only give a rough indication of the actual cluster detection efficiency, since the clusters are not distributed at random within the frames but tend to clump together in ways that are not easily modeled.

The main concern is contamination of the cluster lists by other objects, of which blends of stars in crowded regions is the most serious problem. This effect is expected to be more severe at fainter magnitudes, possibly causing the slopes of the luminosity functions to be overestimated, and is considered below (Sect. 4.3). Another potential problem is that some clusters might be more compact than the adopted size limit and therefore would not be counted as clusters, but to first order this should not lead to any systematic errors in LF slopes because the linear sizes of star clusters are nearly independent of their masses/luminosities (e.g. Janes, Tilley, & Lyngå 1988; Testi, Palla, & Natta 1999; Zepf et al. 1999).

Background objects, especially early-type galaxies, might also resemble star clusters. To test how many such objects would typically be expected in the relevant magnitude range within the WFPC2 field, F606W exposures of two reference fields were downloaded and reduced in the same way as the galaxy data. One field was the *Hubble Deep Field* (Williams et al. 1996), of which 7 exposures with a total exposure time of 6300 s were used, making it much deeper than any of the galaxy datasets. The other field was a parallel WFPC2 exposure located 175' from NGC 628 (Program ID 9244), exposed for 500 + 260 s in F606W and thus of about the same depth as the galaxy datasets. In the HDF and NGC 628 reference fields, a total of 10 and 13 objects brighter than  $V = 23$  and 5 and 6 objects brighter than  $V = 22$  were found, of which only about half met the size criterion used for cluster selection. In the presence of dust extinction in the cluster host galaxies, these numbers would be further reduced. The density of distant background galaxies may vary across the sky, but contamination by background galaxies is clearly not expected to pose any significant problem unless a rich galaxy cluster happens to be in the background.

Fig. 5 shows a  $(B-V, U-B)$  two-color diagram for cluster candidates in NGC 6946 with  $UBV$  photometry (Table 4), corrected for Galactic foreground reddening. The solid curve superimposed on the plot represents the mean colors of LMC clusters (Girardi et al. 1995) while the dashed line is a 4 Myr solar metallicity stellar isochrone from Girardi et al. (2002). There are a few objects with redder colors than expected, which could be highly reddened clusters or possibly background galaxies, but the majority of the cluster candidates have colors that are compatible with the LMC

clusters. Although the location of the bluest clusters in the  $(B-V, U-B)$  plane is not very different from that of individual early-type stars, the fact that most of the cluster candidates fall near the expected location provides a good sanity check on the identifications.

The color distributions for cluster candidates in fields with photometry in more than one band are compared in Fig. 6. The information contained in a single color is limited, but slight differences between the fields do exist and are most likely due to different reddening and/or age distributions. In particular, the broader  $V-I$  color distribution in the NGC 5236 field may suggest larger variations and a higher mean reddening in this field compared to NGC 6946-3. However, multi-color data are needed to resolve the age-reddening degeneracy.

## 4.2. Reddening

For clusters with complete  $UBV$  photometry, an estimate of the individual reddenings can be obtained using the “ $Q$ ”-method (van den Bergh & Hagen 1968, hereafter VH68), where the intrinsic color (e.g.  $(B-V)_0$ ) of the cluster is assumed to be a function of the reddening-free  $Q$ -parameter. The reddening  $E(B-V)$  is then  $E(B-V) = (B-V)_{\text{obs}} - (B-V)_0$ , and can be converted to e.g.  $A_V$  using the reddening law in Cardelli, Clayton and Mathis (1989),  $A_V = 3.0 E(B-V)$ .

According to VH68,  $Q = (U-B) - 0.75 \times (B-V)$ , is related to the intrinsic color  $(B-V)_0$  of a cluster as  $(B-V)_0 = 0.78 \times Q + 0.40$ . Comparison with population synthesis models (Bruzual & Charlot 2001, priv. comm., hereafter BC2001) shows that a shallower relation,

$$(B-V)_0 \sim 0.24 Q + 0.21 \tag{1}$$

provides a better fit over most of the range in  $Q$  (Fig. 7). The range over which Eq. 1 provides a reasonable fit to the models is  $10 \text{ Myr} \lesssim \text{age} \lesssim 400 \text{ Myr}$ , according to the BC2001 models. It is, however, important to note that the relation is strictly valid only for intermediate  $Q$  values. For  $Q \lesssim -0.65$ , corresponding to ages below  $\sim 30 \text{ Myr}$ ,  $B-V$  (or any other color) is no longer a simple function of  $Q$  and the  $Q$ -method may underestimate  $A_V$  by up to  $\sim 1 \text{ mag}$  for the youngest clusters. The situation is further complicated by the fact that the shape of the “loop” in the colors of the youngest clusters is strongly metallicity-dependent. A similar effect exists for  $Q \gtrsim -0.3$  (age  $\gtrsim 160 \text{ Myr}$ ), although the effect would here be to grossly overestimate the reddenings.

Figure 8 shows plots of  $A_V$  vs.  $Q$  parameter (a) and  $V$  magnitude (b) for the clusters in Table 4. The horizontal dashed line indicates the Galactic foreground reddening towards NGC 6946, which is  $A_B = 1.48 \text{ mag}$  or  $A_V = 1.11 \text{ mag}$  according to Schlegel et al. (1998). The plots do show some clusters with apparently very large reddenings, but for most clusters the observed reddenings are compatible with the Galactic foreground values and the internal absorption in NGC 6946 generally appears to be less than about  $1 \text{ mag}$  in  $A_V$ . Similar conclusions can be reached from inspection of Figure 5. For some clusters the derived reddenings are actually smaller than the foreground value, which might be partly due to the ambiguity in the reddening determinations for the youngest



clusters. Another uncertainty arises from stochastic color variations, especially in low-mass clusters where the integrated light is dominated by a few individual stars (Girardi et al. 1995). The results obtained here do, of course, not necessarily give a representative picture of the situation in the other fields, but they are suggestive that most clusters are subject only to modest reddenings.

### 4.3. Luminosity functions

The LFs of cluster candidates in each galaxy are shown in Figs. 9 and 10. Solid line histograms represent the raw, uncorrected LFs, whereas the dotted and dashed lines show the LFs after visual inspection of the cluster samples and removal of potential contaminants (see below). Superimposed on each panel is a dotted-dashed line representing a power-law fit of the form

$$dN(L_V)/dL_V = \beta L_V^\alpha \quad (2)$$

to the raw, uncorrected luminosity distributions. In the following the subscript “ $V$ ” will generally be omitted. For comparison, data for LMC clusters taken from Bica et al. (1996) have also been included. According to Bica et al. (1996), their catalog is complete to about  $V = 13$  or  $M_V \approx -6$ , assuming a distance modulus of 18.5.

The data in Figs. 9–10 are rather inhomogeneous in terms of absolute magnitude coverage, partly because the galaxies are at different distances and partly because of the different exposure times. The various fits have exponents between  $\alpha \sim -2.0$  and  $\alpha \sim -2.4$ , with a tendency for the slopes to get steeper for cluster samples that span brighter magnitude intervals. However, a hint of a bend in the LF is seen directly in the data only for NGC 1313 and perhaps NGC 5236. The lines drawn for these two galaxies represent fits to clusters with  $-8 < M_V < -6$ . The LF slopes are consistent with data for NGC 3627 presented by Dolphin & Kennicutt (2002), who estimated  $\alpha = -2.53 \pm 0.15$  for young clusters with  $-11 < M_V < -8$  in that galaxy. Elson & Fall (1985) found a shallower slope of  $\alpha = -1.5$  for the LF of LMC clusters, based on eyeball estimates of the integrated magnitudes for a sample of 137 clusters, but the Bica et al. (1996) data indicate a slope of about  $\alpha = -2$ , compatible with the range of values found for the other galaxies studied here.

Table 5 lists the parameters for the LF fits, given in two different formats. The magnitude intervals used for the fits and the number of clusters in each interval are given in columns (2) and (3). The  $a$  and  $b$  values (columns 4 and 5) are the coefficients in a fit of the form

$$\log \Sigma_{\text{cl}} [\text{kpc}^{-2} \Delta \text{mag}^{-1}] = b + a M_V \quad (3)$$

where  $\Sigma_{\text{cl}}$  is the surface density of clusters (clusters per magnitude bin per  $\text{kpc}^{-2}$ ).  $\alpha$  and  $\beta$  in Eq. (2) and  $a$  and  $b$  in Eq. (3) are related as

$$\alpha = -(2.5a + 1) \quad (4)$$

and

$$\beta = -\frac{2.5}{\ln 10} 10^{b+4.8a} \quad (5)$$

for  $L_V$  in units of  $L_\odot$  and  $M_{V,\odot} = 4.8$ . For NGC 1313 and NGC 5236 there are two entries for fits in the range  $-8 < M_V < -6$  and  $-9 < M_V < -7.5$ , respectively. These fits again suggest a steepening at brighter magnitudes, although this is formally detected only at the  $\sim 1\sigma$  level in NGC 1313 and at even lower significance in NGC 5236.

Column (7) gives the surface densities of clusters at  $M_V = -8$  ( $\Sigma_{\text{cl}}^{-8}$ ), based on the LF fits. An absolute magnitude of  $M_V = -8$  is useful as a fiducial point for comparison of the cluster densities because it allows Milky Way and LMC data to be compared with data for more distant galaxies. The cluster densities in Table 5 were obtained simply by normalizing number counts to the WFPC2 field of view, but because the pointings cover different sections of their host galaxies, it should be kept in mind that these cluster densities are not necessarily representative for each galaxy as a whole. Significant local variations are present even within the WFPC2 frames. The data for the Milky Way open cluster luminosity function are taken from van den Bergh & Lafontaine (1984) and refer to the Solar neighborhood, while many of the WFPC2 pointings cover regions closer to the center of the galaxies. The Bica et al. (1996) catalog covers about  $5 \text{ deg} \times 5 \text{ deg}$  of the LMC.

Comparison with the Milky Way data confirms the notion that the cluster system of our Galaxy is comparable to those of other spirals with modest star formation rates (NGC 628, NGC 3184 and NGC 6744), but poorer than that of the LMC and NGC 6946 (see Table 6 for  $\Sigma_{\text{SFR}}$  values). It is also worth noting that the LMC cluster system by no means appears to be extreme. Although richer than that of the Milky Way, it falls short of galaxies like NGC 1313, NGC 5236 and NGC 6946. It is interesting (though hardly surprising) to note that  $\Sigma_{\text{SFR}}$  and  $\Sigma_{\text{cl}}^{-8}$  scale with each other. A conclusion as to whether or not the relation is linear is, however, not really warranted by the current data, but other studies suggest that the efficiency of cluster formation relative to field stars increases with  $\Sigma_{\text{SFR}}$  (LR2000). Specifically, Billett, Hunter & Elmegreen (2002, hereafter BHE02) found that the total  $U$ -band luminosity of all clusters  $L(U)$  normalized to the galaxy area  $A$  scales with  $\Sigma_{\text{SFR}}$  as  $L(U)/A \sim \Sigma_{\text{SFR}}^{1.4}$ .

As mentioned above, some of the objects included in the cluster lists may be contaminants. To check how much this effect and completeness issues might influence the LF fits, the datasets were visually inspected and objects suspected to be non-clusters were manually removed from the cluster lists. As an example, this resulted in the removal of 76 out of 370 objects in the three NGC 6946 fields, which were typically located within crowded regions of the images and most likely blends of two or several stars. The dotted and dashed lines in Figs. 9 and 10 show the contamination-corrected LFs, with and without correction for incompleteness. The incompleteness corrections have very little effect on the LF fits, and the vast majority of uncertain cluster identifications are in the faintest bins. Some of the objects that were rejected during the visual inspection might be real clusters, so the dashed lines may be considered a pessimistic estimate of the contamination. In most cases the LF fits were not strongly affected by the visual inspection and removal of suspected contaminants, with the  $\alpha$ -values typically becoming flatter by  $\sim 0.1$ . The contamination corrections might bring the slopes of some of the observed LFs closer to that of the LMC. The changes in  $\Sigma_{\text{cl}}^{-8}$  were also modest, generally resulting in a decrease of less than  $\sim 25\%$  relative to the values in

Table 5. One galaxy where the visual inspection caused significant depletion at the faint end of the LF is NGC 1313, but note that the limiting magnitude in this galaxy is fainter than in most of the other galaxies studied here. This, combined with significant crowding in the central pointing (where most cluster candidates are located), made the identification of many of the faintest sources in this galaxy ambiguous.

## 5. Brightest clusters - physics or sampling statistics?

### 5.1. Relations between maximum cluster luminosities and galaxy properties

BHE02 suggested a relation between  $\Sigma_{\text{SFR}}$  and the maximum mass  $M_{\text{max}}$  of a star cluster that can form in a galaxy, based on the correlation between gas density and star formation rate (Kennicutt 1998) and the assumption of pressure equilibrium between cluster-forming cloud cores and the ambient interstellar medium. The predicted relation is of the form

$$M_{\text{max}} \propto \Sigma_{\text{SFR}}^{\eta} \quad (6)$$

where  $\eta = 2$  for constant cluster *density* (the case considered by BHE02) and  $\eta = 2/3$  for constant cluster *size*. Although observations show that any correlation between linear sizes and masses of star clusters is weak, if present at all, it is unclear whether the same is true for the proto-cluster cloud cores. For example, Ashman & Zepf (2001) have suggested that the absence of a size-mass relation for clusters could be at least partly due to a higher star formation efficiency in more massive clouds, causing low-mass clusters to expand more than high-mass clusters after the gas is blown away. Depending on the importance of such effects,  $\eta$  might have values anywhere between the two extremes of  $2/3$  and  $2$ .

If the mass of the most massive cluster is always regulated by physical processes in the interstellar medium, the exponent  $\eta$  might in principle be determined by plotting  $M_{\text{max}}$  versus  $\Sigma_{\text{SFR}}$  for a sample of galaxies. However, if the total cluster population is too small then  $M_{\text{max}}$  may never be realized and the maximum observed cluster mass observed in a galaxy will instead be the result of random sampling from the mass function. In most cases information about the masses of individual clusters is not available, at least not with sufficient accuracy, and one is instead restricted to studying luminosity- rather than mass distributions. Because only a small fraction of the most massive clusters in a galaxy with an extended star formation history will also be very luminous, the luminosity of the brightest cluster in a galaxy might be limited by sample statistics, even if the mass of the most massive cluster is not.

The aim of this section is to investigate under what circumstances the luminosity of the brightest cluster is determined by either physics or statistics. Let us assume for now that there is a universal cluster luminosity function of the form (2) and that the normalization ( $\beta$ ) is proportional to the area-normalized star formation rate  $\Sigma_{\text{SFR}}$  to some power  $\gamma$ , and the galaxy area  $A$ , i.e.

$$dN(L)/dL = c A \Sigma_{\text{SFR}}^{\gamma} (L/L_{\text{ref}})^{\alpha}. \quad (7)$$

In practice it is convenient to normalize the LF at a reference luminosity,  $L_{\text{ref}}$ , rather than at  $1 L_{\odot}$ , since  $c$  will otherwise depend strongly on  $\alpha$ . The luminosity of the brightest cluster  $L_{\text{max,stat}}$  expected from random sampling of the LF can then be estimated as in BHE02 by requiring

$$c A \Sigma_{\text{SFR}}^{\gamma} \int_{L_{\text{max,stat}}}^{\infty} (L/L_{\text{ref}})^{\alpha} dL = 1, \quad (8)$$

i.e.

$$L_{\text{max,stat}} = \left[ -\frac{c}{\alpha + 1} \left( \frac{A}{\text{kpc}^2} \right) \left( \frac{\Sigma_{\text{SFR}}}{10^{-3} M_{\odot} \text{yr}^{-1} \text{kpc}^{-2}} \right)^{\gamma} \left( \frac{L_{\text{ref}}}{L_{\odot}} \right)^{-\alpha} \right]^{-1/(\alpha+1)} L_{\odot}, \text{ for } \alpha < -1. \quad (9)$$

Eq. (9) allows the maximum cluster luminosity expected from random sampling of the LF to be estimated when  $\Sigma_{\text{SFR}}$ ,  $A$  and the normalization constant  $c$  are known. The last column in Table 5 lists  $c$  values for  $\alpha = -2.4$ ,  $\gamma = 1.0$ ,  $L_{\text{ref}} = 1.32 \times 10^5 L_{\odot}$  ( $M_V = -8$ ) and the observed cluster surface densities at  $L_{\text{ref}}$ . The average is  $c \sim 7.4 \times 10^{-6}$ , or  $c \sim 5.5 \times 10^{-6}$  for  $\gamma = 1.4$ . All galaxies except NGC 5236 fall well within a factor of 2 from this normalization, even though  $\Sigma_{\text{cl}}^{-8}$  and  $\Sigma_{\text{SFR}}$  both vary by an order of magnitude. When calculating the normalization constants it was ignored that the cluster densities in Table 5 may be somewhat overestimated because of contamination, but because of the overall uncertain nature of the contamination and completeness corrections, it was decided to simply use the LF fits in Table 5 at face value.

Direct extrapolation of a power-law luminosity function with  $\alpha = -2.4$  from the local surface density of clusters near the Sun at  $M_V \approx -8$  (van den Bergh & Lafontaine 1984) indicates that the brightest cluster within  $\approx 2$  kpc from the Sun should have  $M_V \approx -9.6$ . This is quite compatible with the observations, since the brightest open clusters within this distance have  $M_V \approx -10$  (e.g.  $h$  and  $\chi$  Per). If the density of open clusters throughout the disk of our Galaxy is as high as in the Solar neighborhood then the brightest cluster expected in the Galaxy as a whole should have  $M_V \approx -12$ .

## 5.2. Comparison with observations

Table 6 lists the surface area  $A$ ,  $\Sigma_{\text{SFR}}$  and  $M_V$  magnitude for the brightest cluster ( $M_V^{\text{max}}$ ) in a sample of nearby galaxies. Most of the galaxies are from LR2000 and BHE02, but data for 5 spirals recently observed at Lick Observatory have also been included. The latter have not previously been published, except for NGC 5194 (Larsen 2000), but the data reduction and cluster selection procedures closely followed the description in Larsen (1999b). Clusters were identified on  $UBV$  images taken with the Prime Focus Camera (PFCAM) on the Shane 3 m telescope, supplemented with  $H\alpha$  data from the 1 m Nickel reflector to eliminate HII regions from the sample. For some of the galaxies in the BHE02 sample the brightest cluster magnitudes are given in the  $R$  rather than  $V$  band. In these cases a  $V - R$  color of 0.2 has been assumed, corresponding to a cluster age between  $10^7$  and  $10^8$  years (BC2001). Galaxy areas are calculated using the  $\log D_0$  values given in the RC3

catalog and star formation rates are based on either IRAS far-infrared fluxes (LR2000, Lick data) or  $H\alpha$  (BHE02). For the BHE02 galaxies, the galaxy areas have been corrected to account for the fact that only a fraction of the galaxies were searched for clusters.

Figure 11 compares the various predictions for the maximum cluster luminosities, based on galaxy areas and star formation rates, with the data in Table 6. Panels (a) and (b) show the observed brightest cluster magnitudes  $M_V^{\max}$  as function of  $A \Sigma_{\text{SFR}}$  ( $\gamma = 1.0$ ) and  $A \Sigma_{\text{SFR}}^{1.4}$  ( $\gamma = 1.4$ ) and straight lines representing the relation expected from random sampling of the LF (Eq. 9) for  $\alpha = -2.4$ . Panel (c) shows  $M_V^{\max}$  vs.  $\Sigma_{\text{SFR}}$  and lines corresponding to  $\Sigma_{\text{SFR}}^{2/3}$  and  $\Sigma_{\text{SFR}}^2$ . Panels (a) and (c) are similar to the two upper panels in Fig. 16 of BHE02, except that the normalizations of the random sampling predictions are here based on the data in Table 5 and the addition of the Lick data. Also note that the normalization in panel (c) is arbitrary. Physically, the normalization of this relation depends on the relation between  $\Sigma_{\text{SFR}}$  and the pressure in cluster-forming cloud cores, and is not easily quantified. If the two outliers NGC 1569 and NGC 1705 are excluded, least squares fits to the datapoints in panels (a) and (b) in Fig. 11 yield slopes corresponding to  $\alpha = -2.55 \pm 0.14$  and  $\alpha = -2.84 \pm 0.18$  for  $\gamma = 1.0$  and  $\gamma = 1.4$ , respectively. The standard deviations around the fits are 0.85 mag and 0.89 mag. In panel (c) the best-fitting power-law is  $L_{\max} \propto \Sigma_{\text{SFR}}^{0.76 \pm 0.18}$  with a scatter of 1.49 mag. Thus, the slopes of the relations in panels (a) and (b) in Fig. 11 are consistent with random sampling from luminosity functions similar to those in Table 5, although the fits formally suggest that the bright-end slopes may be somewhat steeper than the  $\alpha = -2.4$  value used here.

It is, however, clear that a comparison based only on the slopes of the observed relations between galaxy properties and maximum cluster luminosities is unlikely to provide strong constraints on the mechanisms responsible for producing highly luminous clusters. The observed slopes are compatible with predictions based both on physical arguments and sampling statistics, but the *scatter* is much reduced when a dependency on  $A$  is included. This suggests that sample statistics play an important role in determining the luminosity of the brightest clusters even in fairly large spirals.

While the slopes of the relations in Fig. 11a,b agree closely with the expectations, the observed maximum luminosities are systematically lower than the predictions. For  $\gamma = 1.0$  and  $\gamma = 1.4$ , the mean offset is 0.92 mag and 0.75 mag, excluding NGC 1569 and NGC 1705. This difference may very well reflect uncertainties in the area normalization of the cluster surface densities, and/or the exponent  $\alpha$ , dust extinction etc. Also, the LR2000 survey excluded clusters with  $H\alpha$  emission and objects located in very crowded regions, introducing a bias against the very youngest and hence most luminous objects. To remove the offset by changing only the cluster densities would require the mean cluster densities within  $D0$  to be a factor of 3 lower than the estimates in Table 5. The only spiral where the spatial distribution of (young) star clusters has been discussed in some detail is M31, where the clusters are strongly concentrated at intermediate distances from the center (Hodge 1979). If the same is the case in the galaxies studied here then one can suspect from Fig. 1 that the mean cluster densities are indeed somewhat lower than inferred from the WFPC2 pointings.

Alternatively, extrapolation of a power-law LF with  $\alpha = -2.85$  from the observed  $\Sigma_{\text{cl}}^{-8}$  would also remove the offset, although this would be incompatible with most of the fits in Table 5. A more complete survey of clusters is necessary in order to establish the relation between  $\Sigma_{\text{SFR}}$ , luminosity functions and the cluster densities with greater certainty.

As pointed out by BHE02 and Whitmore (2001), the two dwarfs NGC 1569 and NGC 1705 both contain a few highly luminous clusters that are much brighter than expected from the general size of their cluster populations. It is interesting to note that these two galaxies fit better into the “pure”  $\Sigma_{\text{SFR}} - L_{\text{max}}$  relation in panel (c). The luminosity function of star clusters in these galaxies might be peculiar and perhaps biased towards high-mass clusters.

### 5.3. The scatter in the observed maximum luminosities

Although the observed behavior of  $L_{\text{max}}$  as a function of  $A$  and  $\Sigma_{\text{SFR}}$  is well accounted for by random sampling of a power-law LF in terms of the slope and, to a lesser extent, the normalization, some scatter remains in Fig. 11. Part of this scatter may be due to uncertainties in the distances ( $d$ ) of the galaxies, but such uncertainties are partly compensated for by the fact that both the observed and predicted maximum cluster luminosities scale with distance:  $L_{\text{max,obs}} \propto d^2 \propto A$ , while  $L_{\text{max,stat}} \propto A^{0.7} \propto d^{1.4}$  (for  $\alpha = -2.4$ ). Thus, even an error of a factor of two in the distance of a galaxy only leads to a deviation of about 0.5 mag in the  $A \Sigma_{\text{SFR}}^\gamma - L_{\text{max}}$  relation, substantially less than the observed scatter. However, for the  $\Sigma_{\text{SFR}} - L_{\text{max}}$  relation there are no such mitigating circumstances to reduce the effect of distance errors since  $\Sigma_{\text{SFR}}$  itself is distance-independent.

To test how much scatter would be expected if the maximum cluster luminosity is the result of random sampling, a set of Monte Carlo simulations were carried out. In each simulation, clusters were picked at random from a population with a power-law luminosity distribution with  $\alpha = -2.4$  until 2000 clusters had been counted in the interval  $-8.5 < M_V < -7.5$ . A histogram of the  $M_V$  magnitudes of the *brightest* cluster encountered in each of 500 such simulations is shown in Fig. 12. The mean and median of the distribution are  $\langle M_V^{\text{max}} \rangle = -14.1$  and  $\text{Med}(M_V^{\text{max}}) = -14.0$ , respectively, while direct integration of the LF (as in Eq. 8) yields  $M_V^{\text{max}} = -13.7$  for a cluster population of this size. The standard deviation is  $\sigma_V = 1.04$  mag, similar to the observed scatter in the upper panels of Fig. 11. If the high-luminosity tail is truncated at  $M_V = -16$ , e.g. by a physical upper limit to the mass spectrum, then the scatter would decrease to  $\sigma_V = 0.81$  mag.

Thus, we find that not only the slopes but also the observed scatter in panels (a) and (b) in Fig. 11 are fully accounted for by random sampling of the LF, and that the scatter increases significantly if the maximum cluster luminosity is plotted as a function of  $\Sigma_{\text{SFR}}$  only. Several lines of evidence therefore suggest that statistical effects related to sample size play an important role in determining the luminosities of the brightest clusters in galaxies.

#### 5.4. A note on masses

Physically, it would be more relevant to compare cluster *mass* functions rather than LFs. However, useful estimates of cluster masses based on integrated photometry require fairly accurate knowledge of ages because mass-to-light ratios are very sensitive to age. For a sample of clusters with a range of ages, the shape of the luminosity function will generally be different from that of the underlying mass function (Meurer et al. 1995; Zhang & Fall 1999).

If the role played by sampling statistics is as important as suggested in section 5.2, it may be difficult to find galaxies that provide large enough samples of clusters to make detection of a physical upper limit to the LF possible. However, it is still possible that physical conditions play a role in shaping the *mass* distributions of cluster systems. For a continuous star formation history, even relatively quiescent galaxies ought to form very massive clusters once in a while if only sampling effects were important. Such massive clusters should be able to survive for long periods of time. The Milky Way does contain a number of rather massive “open” clusters that are several Gyrs old (Friel 1995) and the 2-Gyr old cluster NGC 1978 in the LMC (Fischer, Welch, & Mateo 1992) is another example.

##### 5.4.1. Simulated luminosity functions: The effect of age differences and reddening

A simple illustration of how the luminosity function may differ from the mass function is provided in Fig. 13, which shows a simulated luminosity function for clusters with ages uniformly distributed between  $10^7$  and  $10^9$  years. The mass function was assumed to be a power-law with exponent  $-2$  for  $10^3 < M < 10^5 M_\odot$ . The  $V$ -band mass-to-light ratio was estimated as  $M_V(1M_\odot) = 1.87 \log(\text{age}) - 11.8$ , obtained as a fit to model calculations by BC2001. The slope of the composite luminosity function is clearly steeper than that of the underlying mass distribution, as indicated by the dashed line which is a fit to the interval  $-11 < M_V < -8$  and has a slope of  $\alpha = -2.72$ . If the mass distribution were a single, untruncated power-law then the combined luminosity function would, of course, be a power-law with the same slope. The steeper slope of the LF in Fig. 13 is due to the truncation of the mass function at  $10^5 M_\odot$ , but more subtle effects like a change in the slope of the mass function at a certain mass would have similar consequences.

This type of simulations can also provide some insight into the effect of dust extinction on the observed LFs. Two cases were considered: 1) random extinctions, varying between  $A_V = 0$  and  $A_V = 1$  mag; 2) random extinctions, varying between  $A_V = 0$  and  $A_V = 9 - \log(\text{age})$  for  $7 < \log(\text{age}) < 9$ , as above. The latter case was adopted as an approximation to a probably more realistic situation where the mean extinction decreases with age. With the extinctions added, the clusters become 0.5 mag fainter on the average, so the fitting interval was adjusted to  $-10.5 < M_V < -7.5$  in order to probe the same mass range. For case (1), the slope is virtually unchanged at  $\alpha = -2.69$ , while case (2) gives an even steeper slope of  $\alpha = -2.97$ . This suggests that age-dependent extinction will steepen the LF slopes, but a correction for this effect would require

detailed knowledge about the age distribution of the clusters involved and the variation of mean extinction with age.

#### 5.4.2. Masses for clusters in NGC 6946

*UBV* data allow ages to be derived with reasonable accuracy and masses can then be estimated with help from population synthesis models. Ages for all clusters in Table 4 were derived according to the “S”-sequence calibration in Girardi et al. (1995), which is based on LMC clusters. The metallicity of clusters in NGC 6946 may be different from that of LMC clusters, but metallicity has only a small influence on colors for young objects, except for clusters younger than about  $10^7$  years where the integrated colors are strongly affected by the rapid, strongly metallicity-dependent and poorly understood evolution of red supergiants. For such clusters, a simple relation between broad-band colors and age no longer exists and rather than quoting uncertain age estimates they are simply listed as  $< 10^7$  years in Table 4. Note that S-sequence ages are not strongly affected by reddening – a *V*-band extinction of 1 mag will typically lead to the cluster ages being overestimated by  $\sim 0.2$  dex. Finally, M/L ratios from the BC2001 population synthesis models were used to estimate the mass of each cluster. The models used here assume a Salpeter stellar IMF with a minimum mass of  $0.1 M_{\odot}$ . More realistic IMFs show some flattening below  $0.5 M_{\odot}$  (e.g. Kroupa 2001), which will result in a smaller total mass than for a Salpeter IMF extending to  $0.1 M_{\odot}$ , but this does not affect the relative comparisons performed here.

Fig. 14 shows mass vs. age for the clusters listed in Table 4 and clearly demonstrates that any attempt to derive a meaningful mass distribution requires deeper photometry as well as a much larger sample of clusters. Because of the rapid increase in M/L ratio as a function of age, illustrated by the dashed line, only the most massive clusters are detectable at ages greater than  $10^8$  years or so, and an appropriate mass range can be observed only for the youngest clusters. Essentially no clusters older than about 300 Myrs are detected. Discarding a couple of clusters with very large and uncertain ages, the most massive clusters found in this single WFPC2 pointing have masses on the order of  $2 \times 10^5 M_{\odot}$ , comparable to the masses of the most *luminous* clusters in NGC 6946 as a whole. The observed mass distribution in this field is again most likely limited by sample statistics and offers little insight as to whether or not a real upper limit to the mass distribution of clusters exists in this galaxy.

## 6. Summary

The cluster populations of 6 nearby spiral galaxies have been examined on archive HST/WFPC2 images. Reidentification of cluster candidates selected on ground-based images in previous work suggests a success-rate of roughly 75% for ground-based cluster selection. The ground-based photometry tends to overestimate the brightness of the clusters by up to several tenths of a magnitude,



because other objects than the cluster itself are included within the relatively large apertures used for the ground-based photometry. On the other hand, ground-based colors agree very well with the WFPC2 photometry.

Typical slopes for the cluster luminosity functions  $dN(L)/dL \propto L^\alpha$  studied here are  $-2.4 \lesssim \alpha \lesssim -2.0$ , clearly steeper than the  $\alpha = -1.5$  for the Milky Way open cluster LF found by van den Bergh & Lafontaine (1984) but in good agreement with data for LMC clusters taken from Bica et al. (1996). However, the Milky Way data cover a much fainter magnitude interval and van den Bergh & Lafontaine pointed out that the lack of very luminous clusters in the Milky Way by itself suggests a steepening of the LF at the bright end. There is a general tendency for fits covering brighter luminosity intervals to have steeper slopes, but a direct hint of a change in slope at  $M_V \approx -8$  is seen only in two galaxies (NGC 1313 and NGC 5236), at the  $\lesssim 1\sigma$  level.

The surface densities of clusters ( $\Sigma_{\text{cl}}^{-8}$ ) scale with the area-normalized star formation rates of the host galaxies. Assuming that this scaling is generally valid, the maximum cluster luminosity expected from random sampling of the LF was estimated by extrapolation of a power-law LF with  $\alpha = -2.4$ , scaled to the area  $A$  and  $\Sigma_{\text{SFR}}$  for a sample of galaxies. Both the slope and scatter of the predicted relation agree well with observations by Larsen and Richtler (2000) and Billett, Hunter & Elmegreen (2002), spanning a wide range in  $\Sigma_{\text{SFR}}$  and physical dimensions. The maximum cluster luminosities are, however, overpredicted by about 0.9 mag, possibly because the mean density of clusters in the galaxies is lower than estimated from the HST pointings. Some starburst dwarfs do manage to form clusters that are significantly more luminous than expected from the size of their cluster populations, indicating that the LF of young clusters in these galaxies may be peculiar.

It remains to be verified whether the cluster LF is really universal, concerning the slopes and their dependence on magnitude, as well as the location and even the existence of a “bend” in the LF. Data presented here suggest that a change in slope occurs at  $M_V \sim -8$ , but observations of a similar bend at  $M_V \sim -10.4$  in the “Antennae” suggest a possible dependency on factors such as environment and/or the age distribution of the clusters involved. An interesting point is whether or not the mass distribution observed in young cluster systems can be reconciled with that of old globular clusters (GCs). The low-mass end of the old GC mass spectrum is likely to be strongly affected by dynamical evolution (Fall & Zhang 2001; Vesperini 2000, 2001), but for masses above  $\sim 10^5 M_\odot$  the mass distribution is well approximated by a power-law with slope  $\sim -1.9$  (Kissler et al. 1994; Kissler-Patig et al. 1996; Larsen et al. 2001b). This is somewhat shallower than the slopes of the luminosity functions at bright magnitudes found in this paper, but similar to the faint-end slopes. The interpretation of these differences is complicated by the fact that the LF of a population of clusters with a range of ages is, in general, different from the more fundamental underlying *mass* distribution. In particular, if the mass function has a physical upper limit then the LF of a cluster population with a range of ages will tend to have a steeper slope than the underlying mass distribution. This is well illustrated by the finding that the mass function of Antennae clusters follows a single power-law with  $\alpha = -2$  over the range  $10^4 < M < 10^6 M_\odot$  (Zhang & Fall 1999).

Because random sampling statistics appear to play an important role in determining the luminosity of the brightest clusters observed in galaxies, the role of physical processes in regulating the upper mass limit of star clusters in galaxies is difficult to determine. For galaxies with a continuous star formation history, observations of the cluster *mass* distribution should make it possible to establish with greater certainty how the maximum possible cluster mass depends on host galaxy properties. This, however, would require fairly accurate age estimates for large samples of clusters, down to  $M_V \sim -6$  or fainter. The new Advanced Camera for Surveys on board HST will be very suitable for such studies because of its large field of view and superior sampling compared to WFPC2. An essential ingredient in future surveys should be inclusion of *U* band imaging, which would allow better age estimates as well as providing constraints on cluster reddenings. Multi-color photometry would also make the cluster identifications more secure.

This work was supported by National Science Foundation grant number AST9900732 and by HST grants GO-08715.02-A and AR-09523. This research has made use of the NASA/IPAC Extragalactic Database (NED) which is operated by the Jet Propulsion Laboratory, California Institute of Technology, under contract with the National Aeronautics and Space Administration. I thank J. Brodie, T. Richtler and the anonymous referee for helpful comments.

## REFERENCES

- Arp, H. C. & Sandage, A., 1985, AJ, 90, 24
- Ashman, K. M. & Zepf, S. E. 2001, AJ, 122, 1888
- Bica, E., Clariá, J. J., Dottori, H., Santos Jr., J. F. C., Piatti, A. E., 1996, ApJS, 102, 57
- Billett, O. H., Hunter, D. A., Elmegreen, B. G., 2002, AJ, in press (BHE02)
- Cardelli, J. A., Clayton, G. C. and Mathis, J. S. 1989, ApJ, 345, 245
- Dolphin, A. E. & Kennicutt, R. C., Jr. 2001, AJ, 123, 207
- Elmegreen, B. G. & Efremov, Y. N., 1997, ApJ, 480, 235
- Elson R. A. W., Fall S. M., 1985, PASP, 97, 692
- Fall, S. M. & Zhang, Q. 2001, ApJ, 561, 751
- Fischer, P., Welch, D. L., & Mateo, M. 1992, AJ, 104, 1086
- Friel, E. D. 1995, ARA&A, 33, 381
- Girardi L., Chiosi C., Bertelli G., Bressan A., 1995, A&A, 298, 87
- Girardi, L., Bertelli, G., Bressan, A., Chiosi, C., Groenewegen, M. A. T., Marigo, P., Salasnich, B., & Weiss, A. 2002, A&A, submitted
- Hodge, P. W. 1961, ApJ, 133, 413
- Hodge, P. W. 1979, AJ, 84, 744
- Holtzman, J. A., Burrows, C. J., Casertano, S., et al. 1995, PASP, 107, 1065
- Janes, K. A., Tilley, C., & Lyngå, G. 1988, AJ, 95, 771.
- Karachentsev, I. D., Sharina, M. E. & Huchtmeier, W. K. 2000, A&A, 362, 544
- Keel, W. C. & White, R. E. 2001, AJ, 121, 1442
- Keel, W. C. & White, R. E. 2001, AJ, 122, 1369.
- Kennicutt, R. C. 1998, ApJ, 498, 541
- Kissler, M., Richtler, T., Held, E. V. et al. 1994, A&A, 287, 463
- Kissler-Patig, M., Richtler, T., Hilker, M., 1996, A&A, 308, 704
- Krist, J., and Hook, R. 1997, “The Tiny Tim User’s Guide”, STScI

- Kroupa, P. 2001, MNRAS, 322, 231
- Larsen, S. S. 1999a, PhD thesis, Univ. of Copenhagen
- Larsen, S. S. 1999b, A&A Suppl., 139, 393
- Larsen, S. S. 2000, MNRAS, 319, 893
- Larsen, S. S., and Richtler, T., 2000, A&A, 345, 59
- Larsen, S. S., and Richtler, T., 2000, A&A, 354, 836 (LR2000)
- Larsen, S. S., Brodie, J. P., Elmegreen, B. G., Efremov, Yu. N., Hodge, P. W. and Richtler, T., 2001, ApJ, 556, 801
- Larsen, S. S., Brodie, J. P., Huchra, J. P., Forbes, D. A. and Grillmair, C. 2001, AJ, 121, 2974
- Larsen, S. S., Forbes, D. A., & Brodie, J. P. 2001, MNRAS, 327, 1116
- Meurer, G. R., Heckman, T. M., Leitherer, C., Kinney, A., Robert, C., & Garnett, D. R. 1995, AJ, 110, 2665
- O’Connell, R. W., Gallagher III, J. S., Hunter, D. A., Colley, W. N., 1994, ApJ, 446, 1
- Schlegel, D. J., Finkbeiner, D. P., and Davis, M. 1998, ApJ, 500, 525
- Shapley, H. & Nail, V. McKibben, 1951, AJ, 55, 249
- Stetson, P. B., 1987, PASP, 99, 191
- Testi, L., Palla, F., & Natta, A. 1999, A&A, 342, 515
- van den Bergh, S. & Hagen, G. L. 1968, AJ, 73, 569
- van den Bergh S., Lafontaine A., 1984, AJ, 89, 1822
- Vesperini, E. 2000, MNRAS, 318, 841
- Vesperini, E. 2001, MNRAS, 322, 247
- Whitmore, B. C., Zhang Q., Leitherer C., Fall S. M., Schweizer F., Miller B. W., 1999, AJ, 118, 1551
- Whitmore, B. C., 2001, in: STScI Symposium Series 14, editor: M. Livio (astro-ph/0012546)
- Whitmore, B. C., Schweizer, F., 1995, AJ, 109, 960
- Williams, R. M., Blacker, B., Dickinson, M. et al. 1996, AJ, 112, 1335
- Wyder, T. K., Hodge, P. W., & Cole, A. 2000, PASP, 112, 594

Zepf S.E., Ashman K.M., English J. et al. 1999, AJ, 118, 752

Zhang, Q. & Fall, S. M. 1999, ApJ, 527, L81

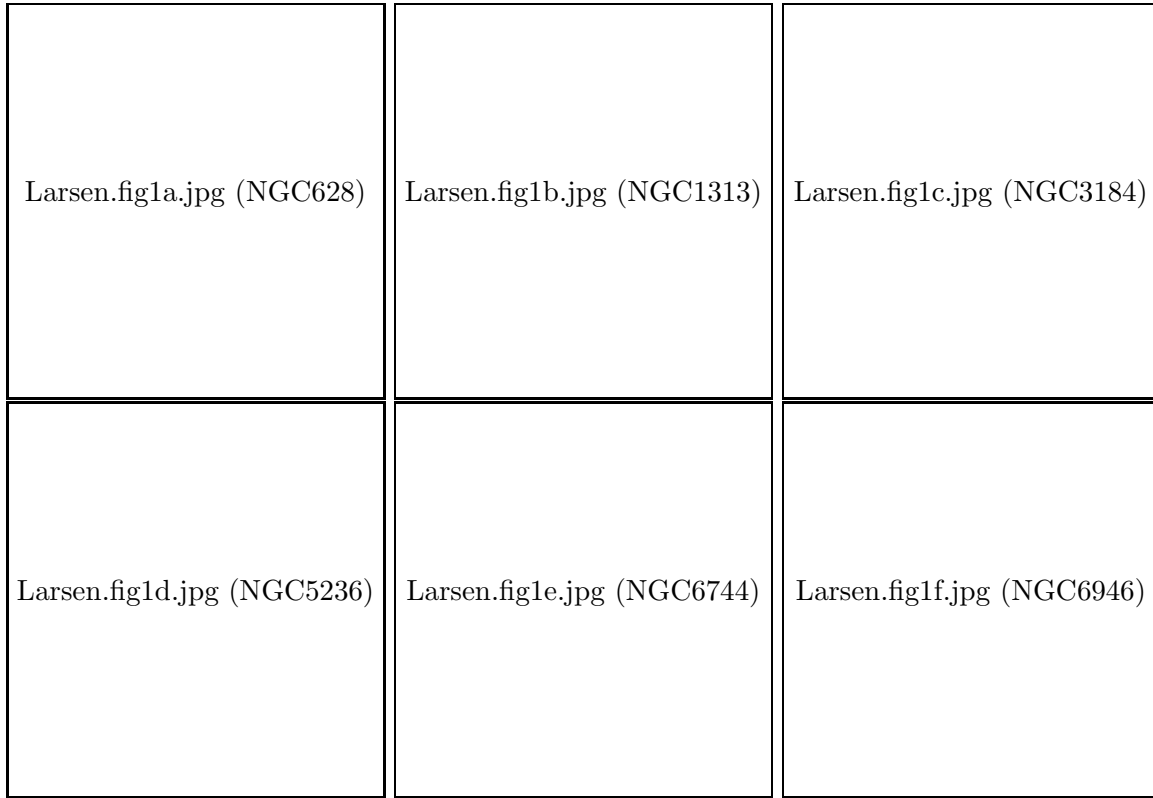


Fig. 1.— WFPC2 pointings used in this paper superimposed on images from the Digitized Sky Survey. Each panel covers  $9' \times 9'$ .

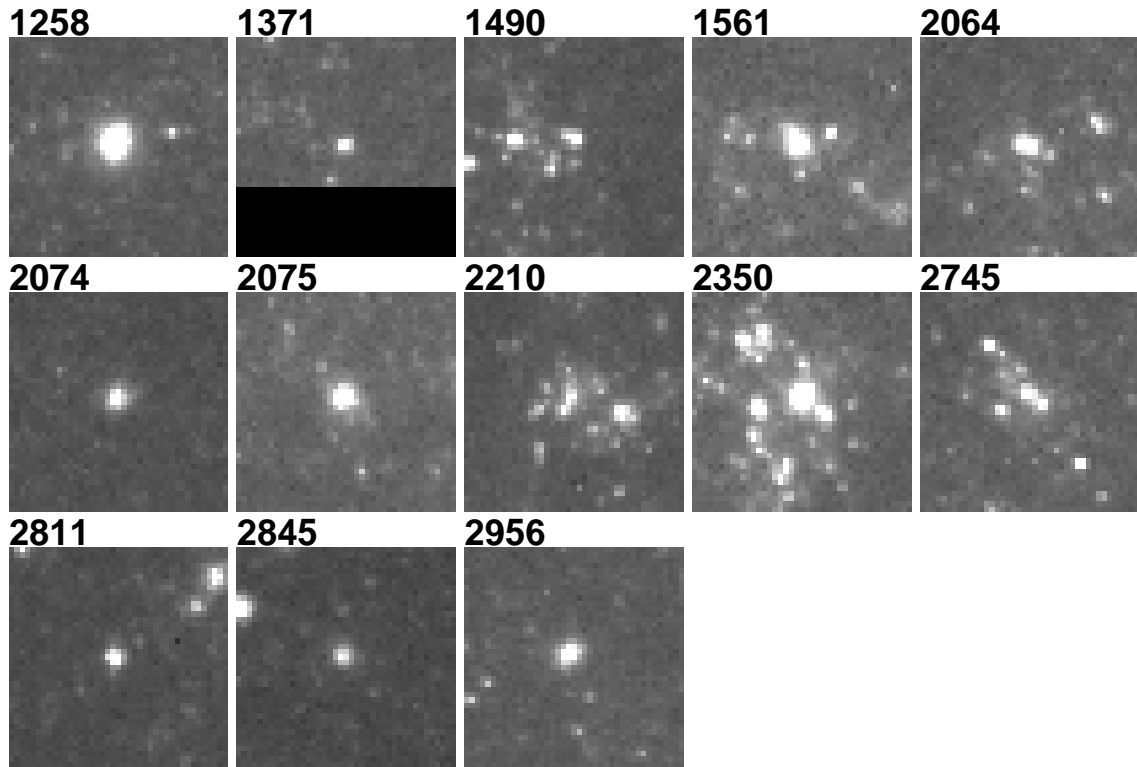


Fig. 2.— HST images of cluster candidates in the NGC 6946–3 field identified on ground-based images

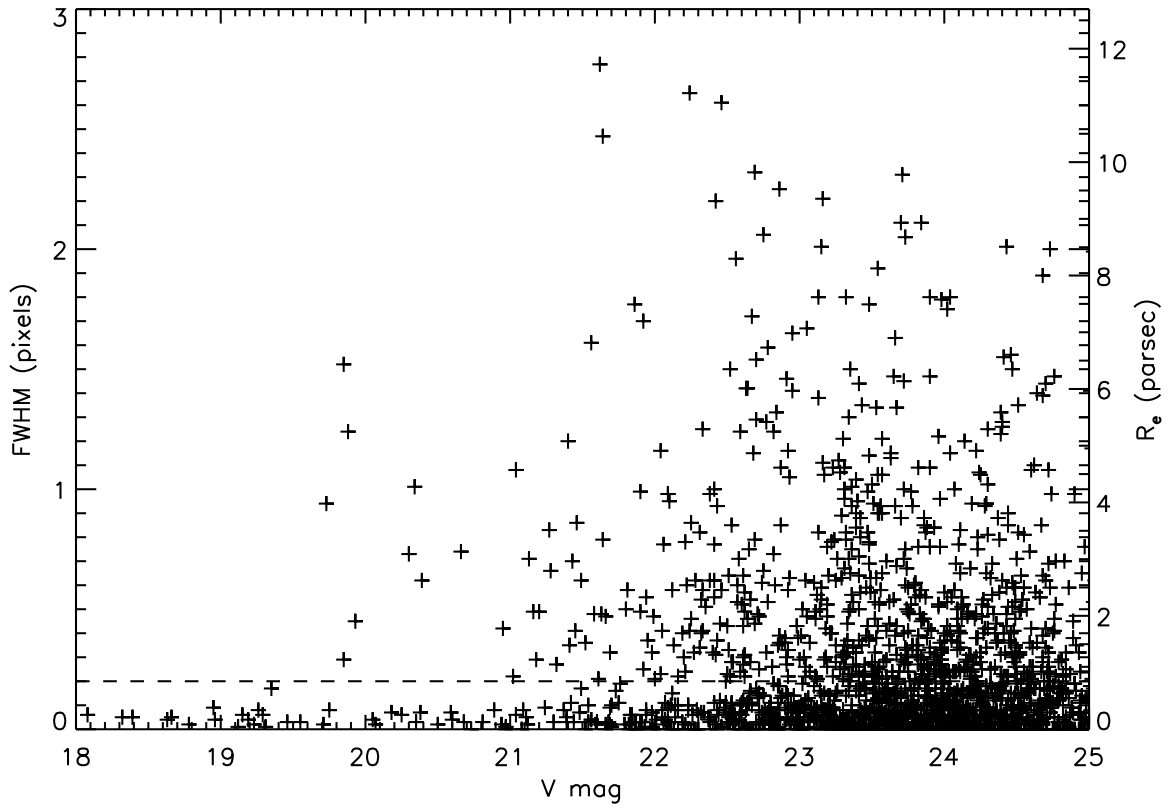


Fig. 3.— Intrinsic FWHM in pixels vs.  $V$  magnitude for sources in field NGC 6946-3.



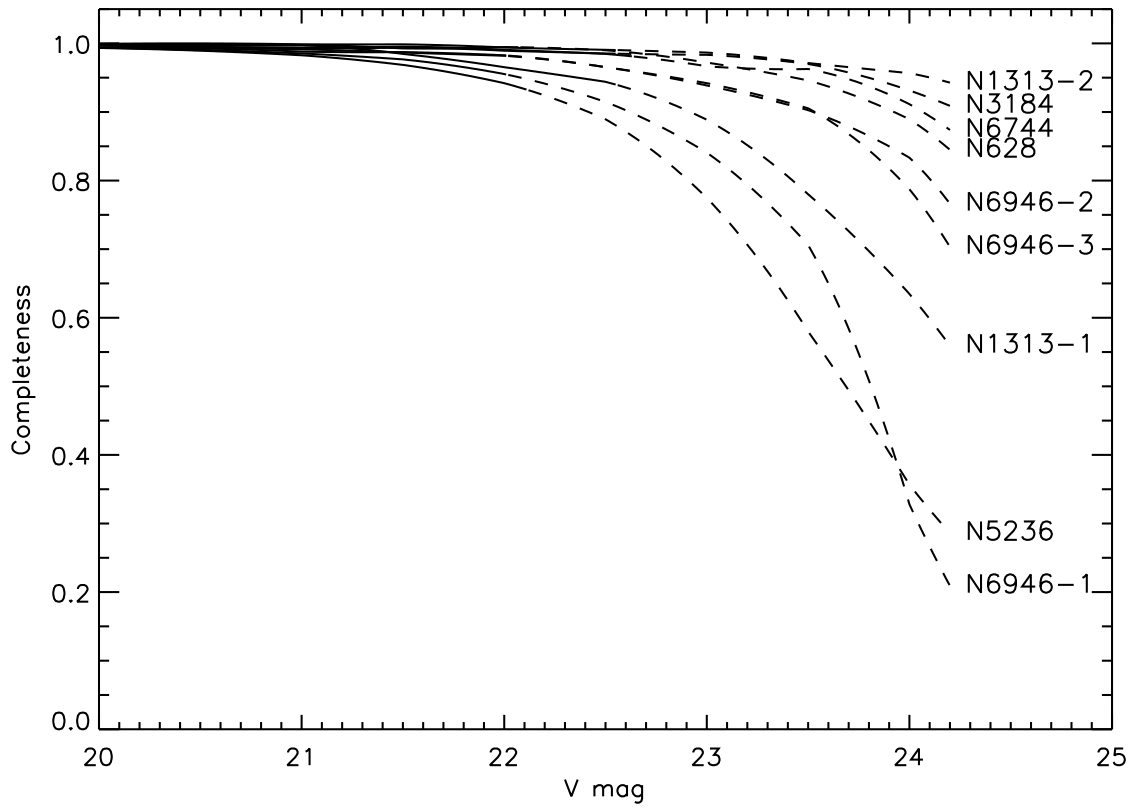


Fig. 4.— Completeness functions for each of the WFPC2 fields, determined from artificial object experiments. The parts of the curves drawn with solid lines represent the magnitude intervals used for luminosity function fits.

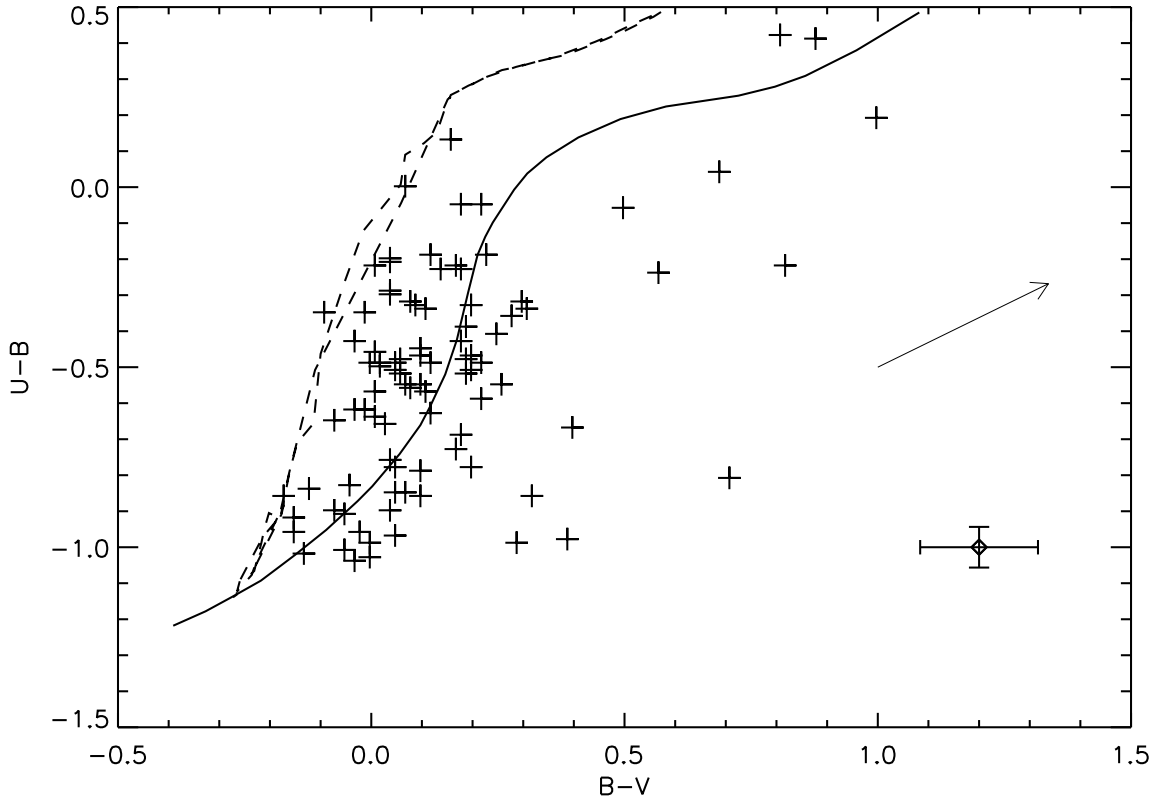


Fig. 5.—  $(B-V, U-B)$  two-color diagram for cluster candidates in NGC 6946, corrected for Galactic foreground reddening. The solid curve is the Girardi et al. (1995) “S”-sequence, representing the mean color of LMC clusters, while the dashed line is a 4 Myr stellar isochrone from Girardi et al. (2002). A typical error bar is shown in the lower right corner and the arrow indicates the reddening vector corresponding to  $A_V = 1$  mag.

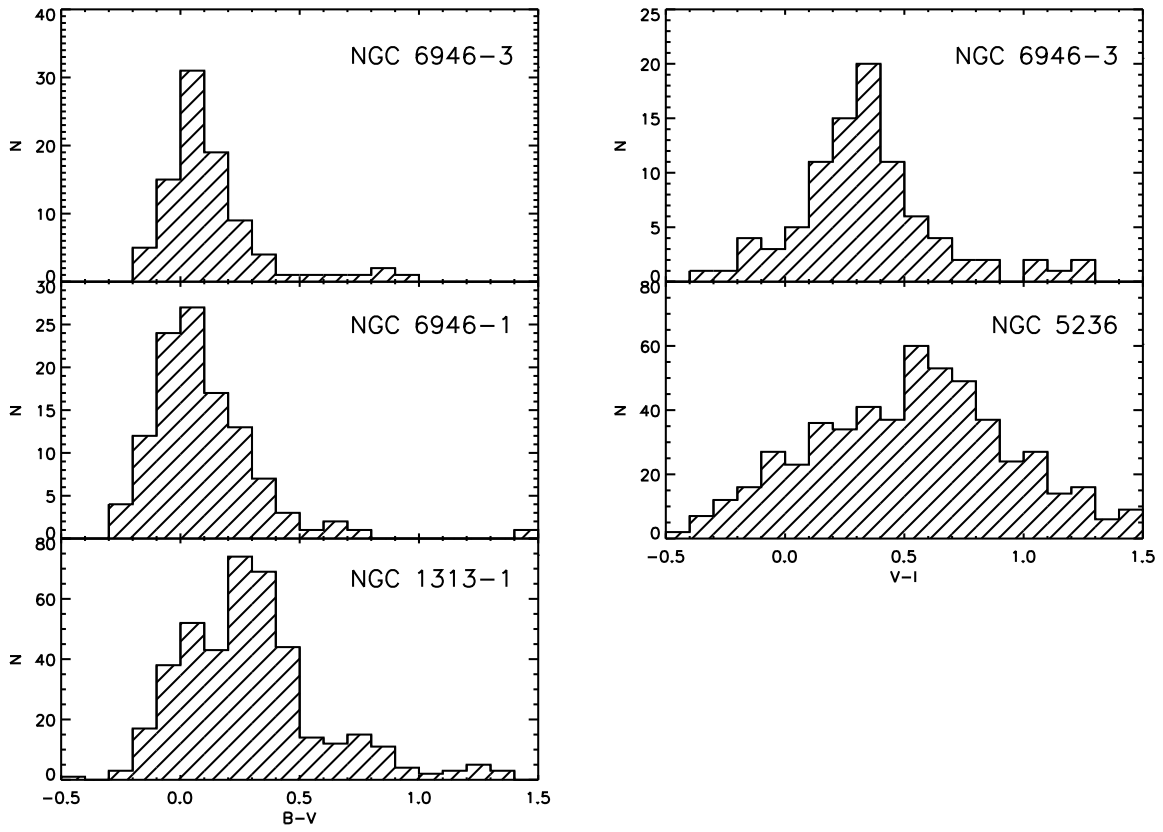


Fig. 6.— Comparison of  $B-V$  (left) and  $V-I$  (right) color distributions for cluster candidates in fields with color information.

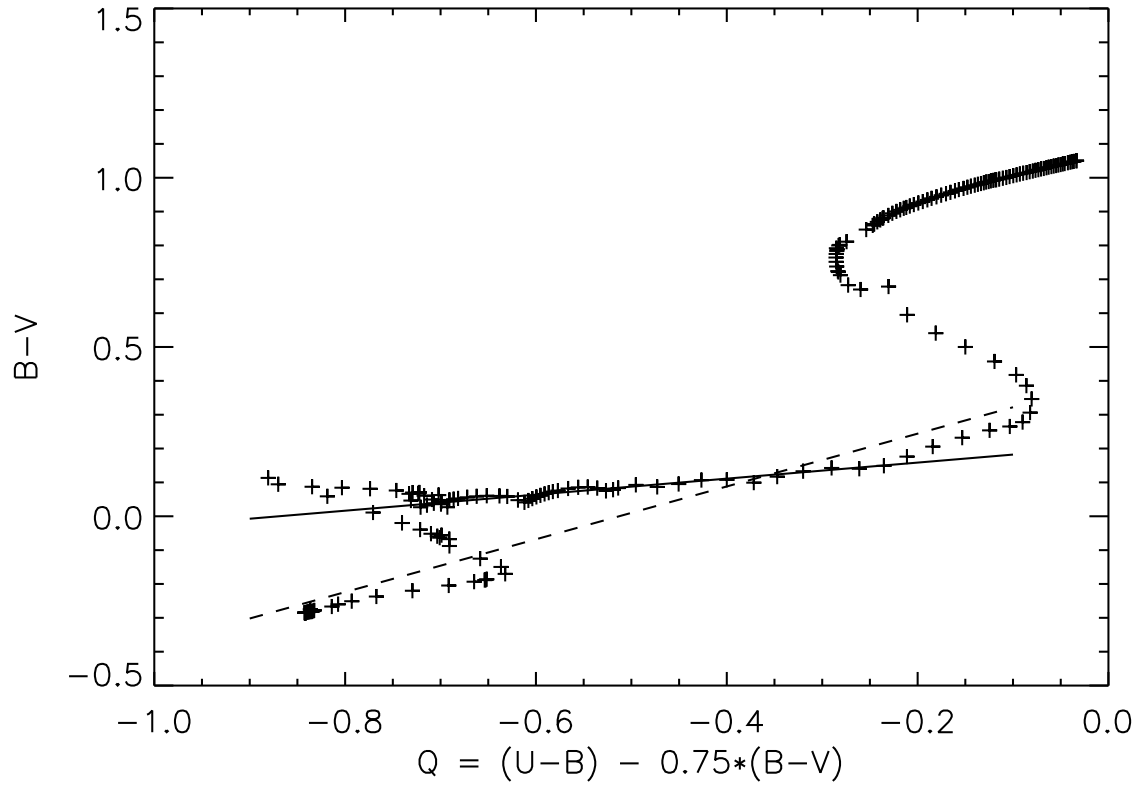


Fig. 7.— Reddening-free  $Q$  parameter vs.  $B-V$  according to BC2001 population synthesis models. The dashed line is the van den Bergh & Hagen (1968) relation, while the solid line is a fit to the model data in the range  $-0.6 < Q < -0.2$  and  $B-V < 0.3$ .

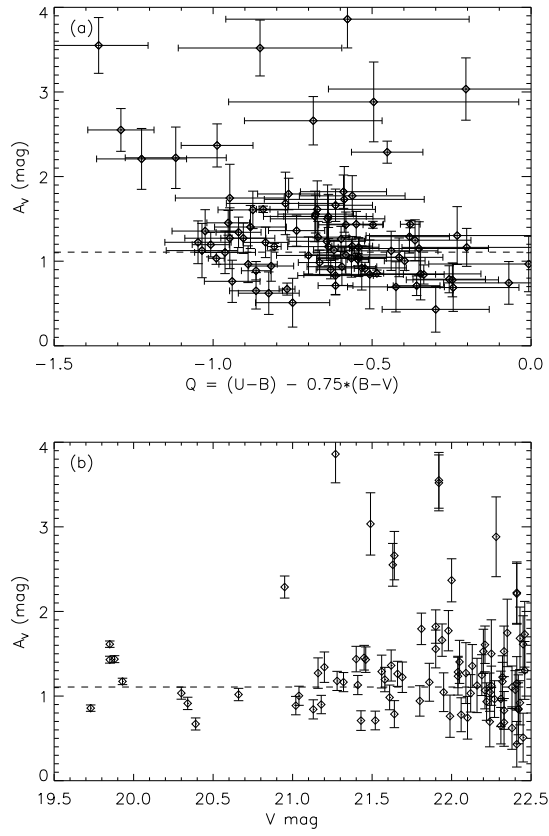


Fig. 8.— Total extinction (in  $V$  mag) towards individual clusters in NGC 6946 listed in Table 4, determined from the Q-method. The  $A_V$  values are shown as a function of Q-parameter (a) and  $V$  magnitude (b). The dashed line indicates the Galactic foreground reddening according to Schlegel et al. (1998).

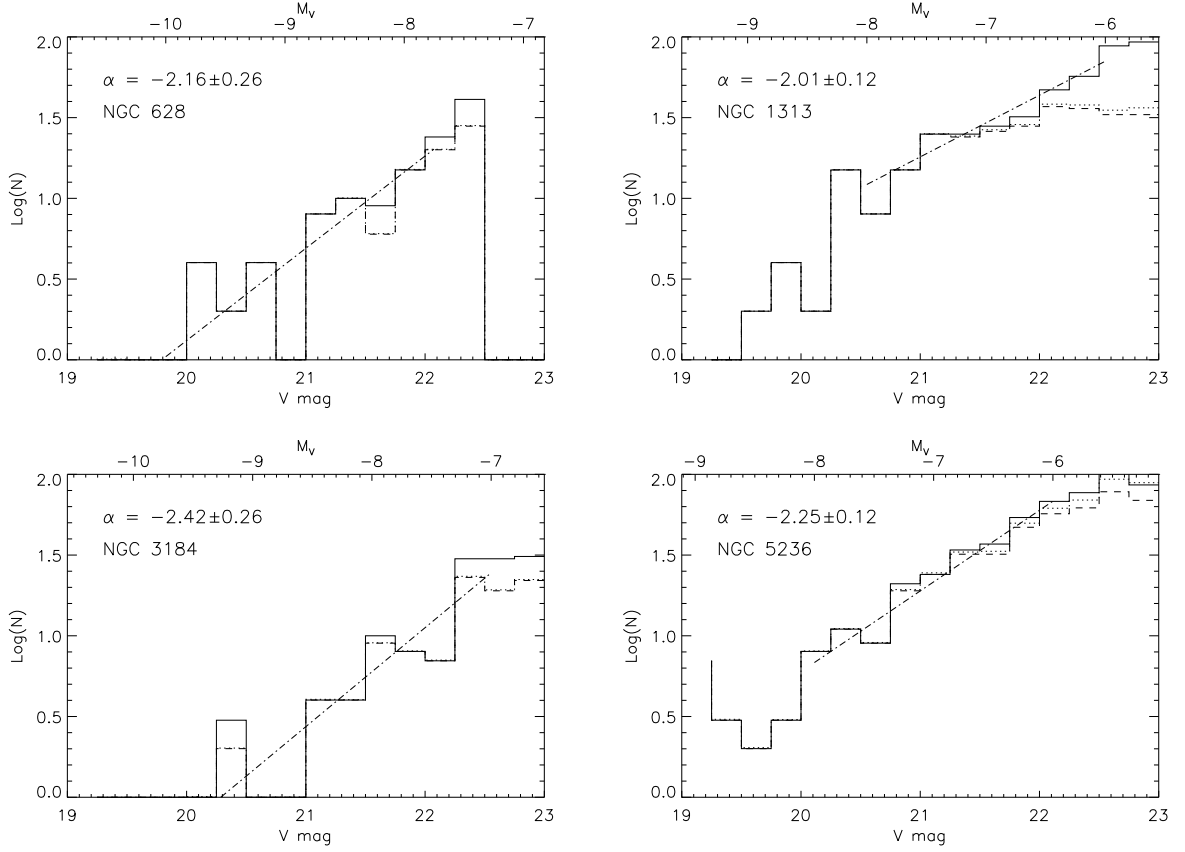


Fig. 9.—  $V$ -band luminosity functions for cluster candidates in the galaxies. Dotted and dashed lines show the luminosity functions after removal of potential contaminants, with and without correction for incompleteness, while the solid lines are the uncorrected LFs. The dotted-dashed lines represent power-law fits of the form  $dN(L)/dL \propto L^\alpha$  to the uncorrected LFs, where the  $\alpha$  values are shown in each panel.

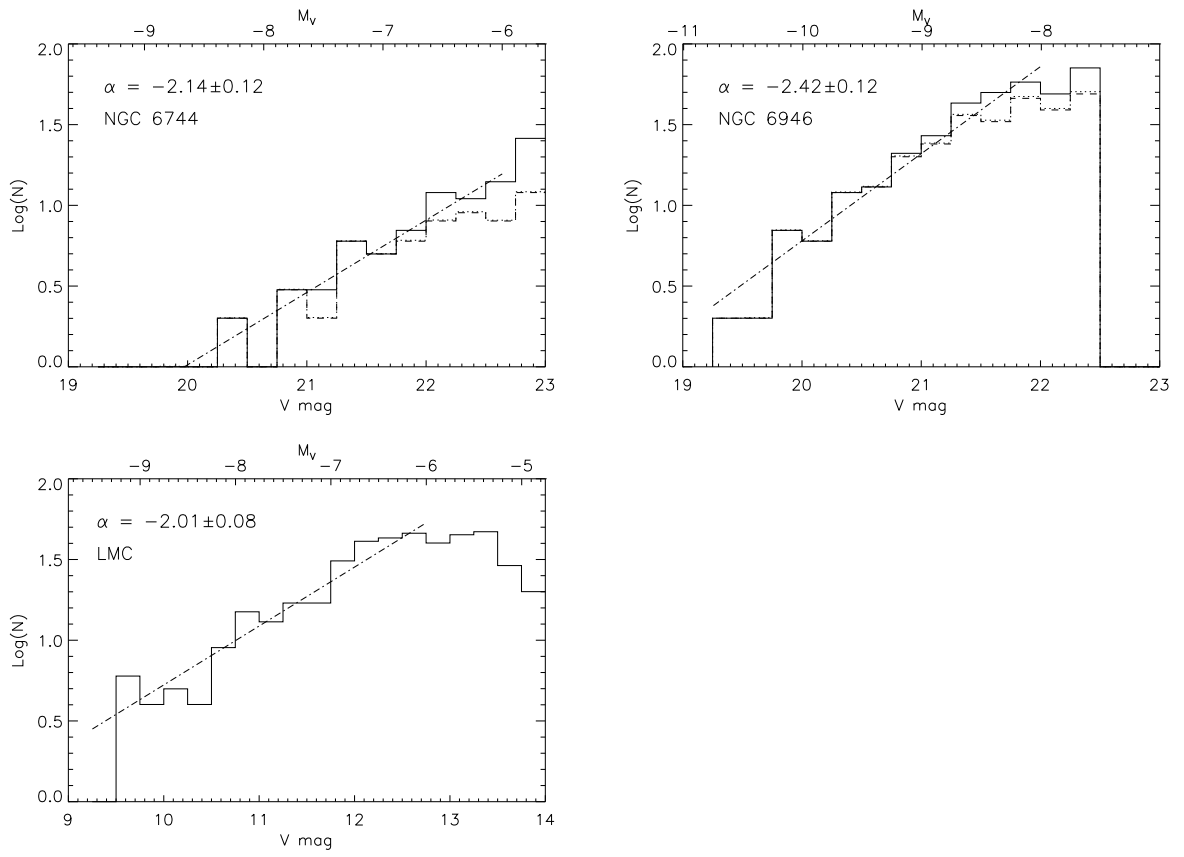


Fig. 10.— See caption to Fig. 9

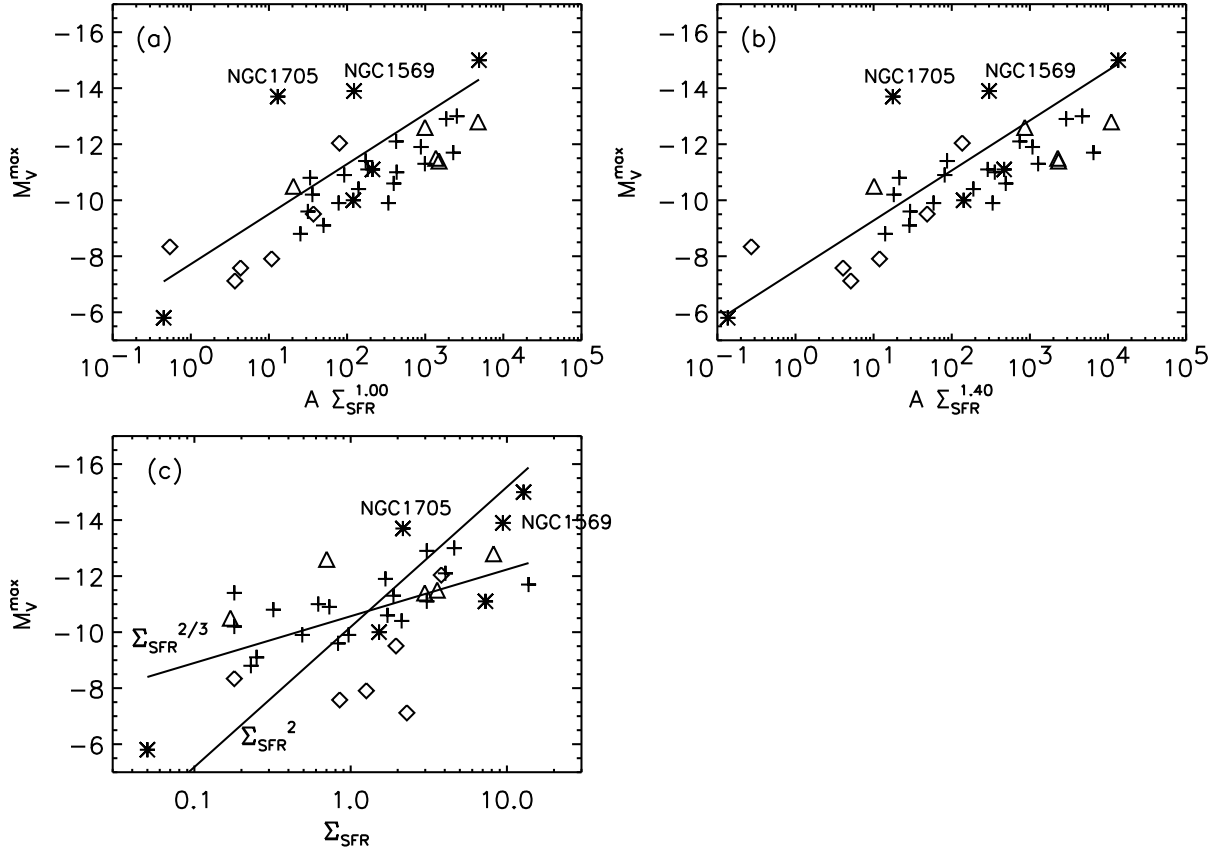


Fig. 11.— Comparison of maximum observed cluster magnitudes with predictions. Panels (a) and (b): maximum magnitudes versus  $A \Sigma_{\text{SFR}}$  and  $A \Sigma_{\text{SFR}}^{1.4}$ . Lines represent predictions based on sample statistics for cluster luminosity function with  $\alpha = -2.4$ . Panel (c): maximum magnitude versus  $\Sigma_{\text{SFR}}$ , with lines representing maximum cluster magnitudes for constant cluster density ( $\eta = -2$ ) or radius ( $\eta = 2/3$ ), according to BHE02. Normalizations of the theoretical relations in panels (a) and (b) come from the data in Table 5 but are arbitrary in panel (c). Symbols : (+) – LR2000, (\*) – LR2000, literature data, (◇) – BHE02, (△) – Lick data.



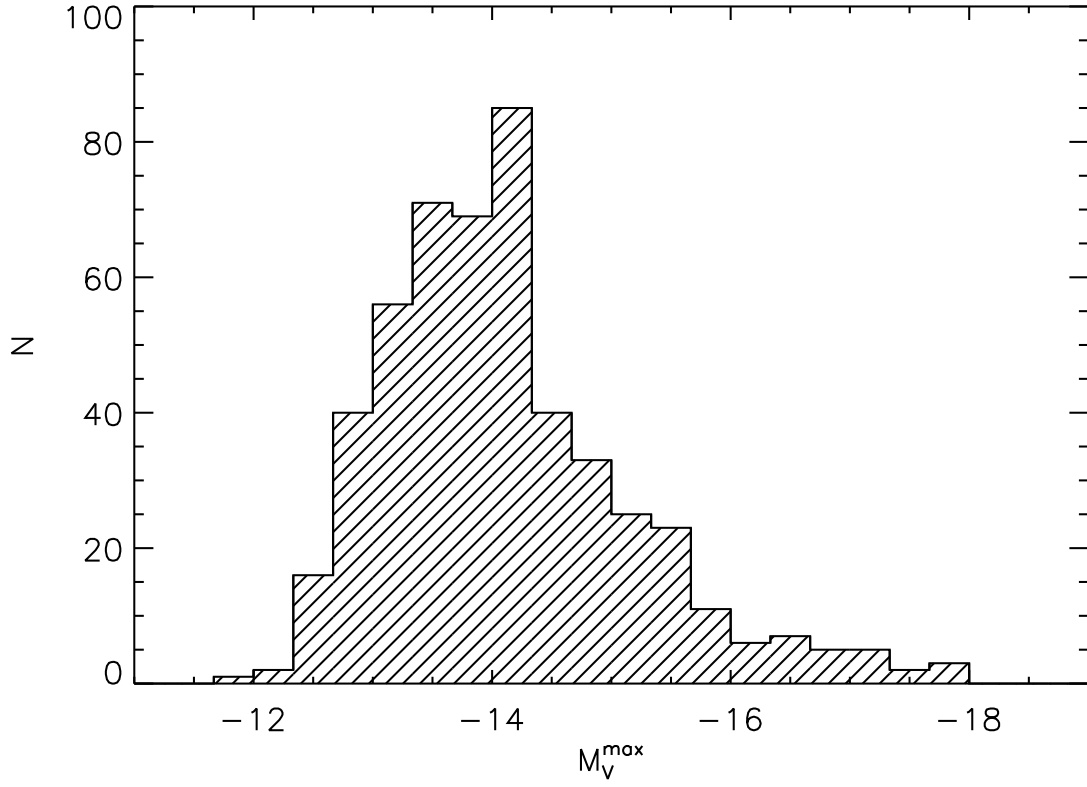


Fig. 12.— Histogram of brightest absolute cluster magnitude for 500 Monte Carlo simulations, assuming random sampling of a power-law luminosity function with  $\alpha = -2.4$ . The cluster population was normalized to 2000 clusters per magnitude bin at  $M_V = -8$ .

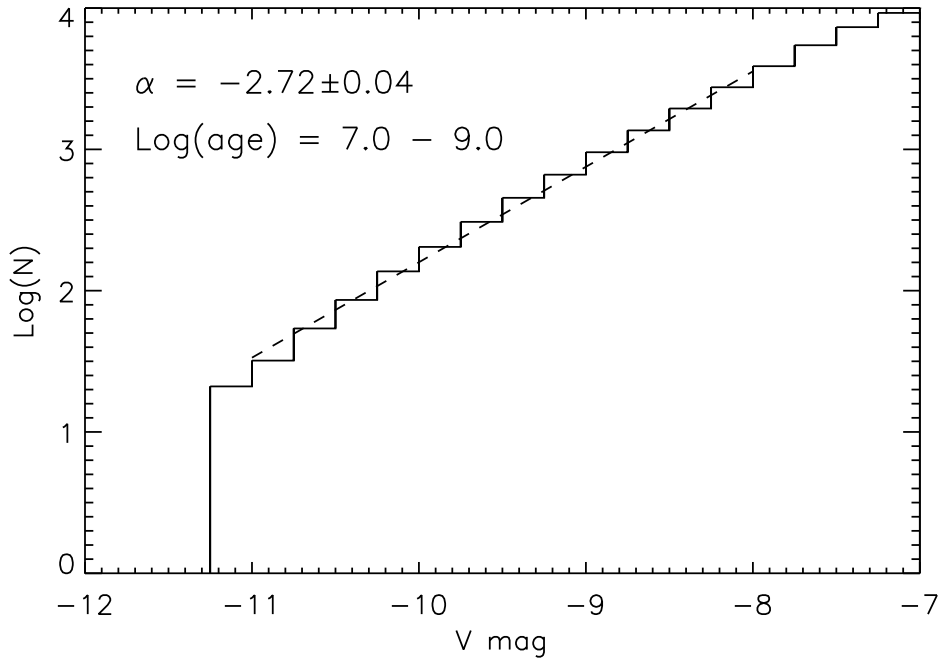


Fig. 13.— Simulated luminosity function for clusters with ages uniformly distributed over the range  $10^7 - 10^9$  years. For the mass function, a power-law with slope  $\alpha = -2.0$  in the interval  $10^3 < M < 10^5 M_\odot$  was assumed. The dashed line represents a power-law fit to the luminosity function in the range  $-11 < M_V < -8$ .

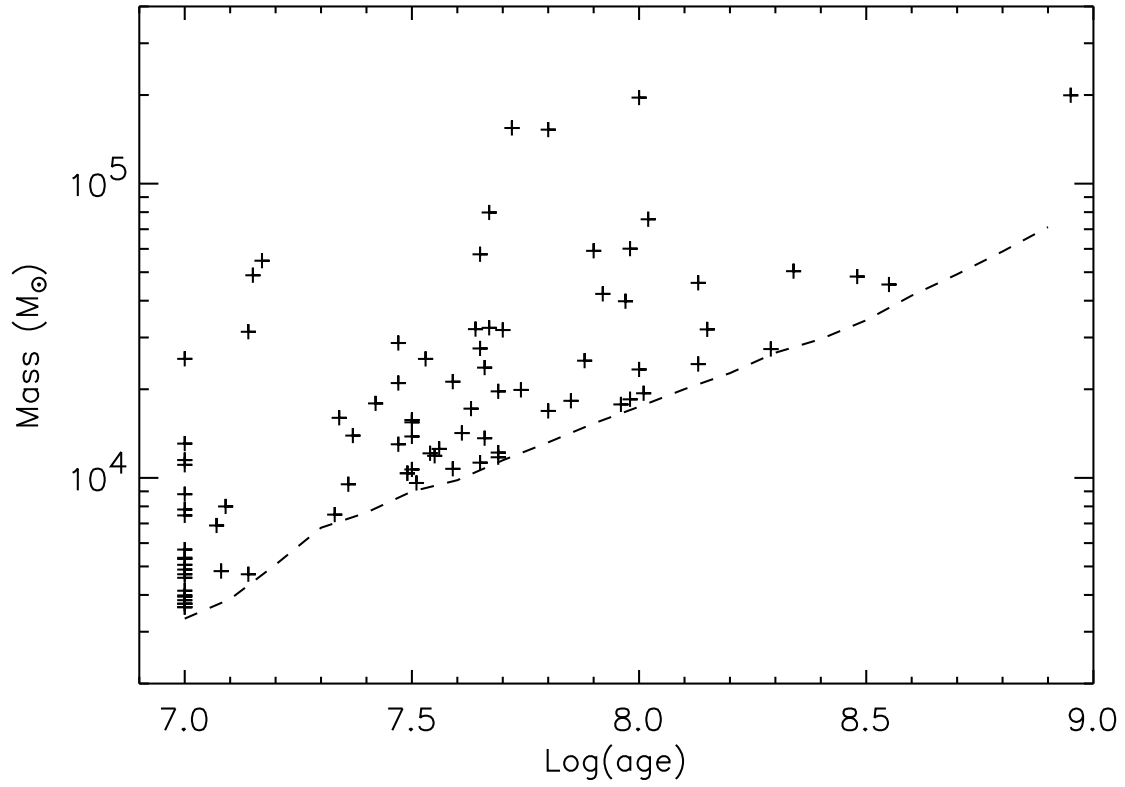


Fig. 14.— Mass vs. age for clusters in NGC 6946 with *UBV* data. The dashed curve indicates the observational cut-off as defined by the magnitude limit and age-dependent M/L ratio.

Table 1. The datasets used in this paper.  $A_B$  values are from Schlegel et al. (1998), retrieved from the *NASA/IPAC Extragalactic Database*. References for the distance moduli  $(m - M)_0$  are given in Section 2.

Field	$A_B$	$(m - M)_0$	Program ID	Exposures
NGC 628	0.30	29.6	8597	F606W (160 + 400 s)
NGC 1313–1	0.47	28.2	9042	F450W ( $2 \times 230$ s), F606W ( $2 \times 230$ s)
NGC 1313–2	-	-	6713	F606W ( $2 \times 300$ s)
NGC 3184	0.07	29.5	8602	F555W ( $2 \times 350$ s)
NGC 5236	0.28	27.9	5971	F606W (1100 + 1200 s), F814W ( $2 \times 1000$ s)
NGC 6744	0.19	28.5	8597	F606W (160 + 400 s)
NGC 6946–1	1.48	28.9	6118	F439W ( $2 \times 400$ s), F555W (400 s)
NGC 6946–2	-	-	8597	F606W (160 + 400 s)
NGC 6946–3	-	-	8715	F336W ( $2 \times 1500$ s), F439W ( $2 \times 1100$ s) F555W ( $2 \times 300$ s), F814W ( $2 \times 700$ s)

Table 2. Aperture corrections for WF images relative to  $r = 5$  pixels, determined from measurements on synthetic images.

$r$	F336W	F439W	F555W	F814W	F336W –F439W	F439W –F555W	F555W –F814W
Point sources							
3.0	0.061	0.053	0.055	0.070	0.008	–0.002	–0.015
20.0	–0.083	–0.078	–0.070	–0.076	–0.005	–0.008	0.006
King $c = 30$ , FWHM = 0.5 pixels							
3.0	0.152	0.149	0.151	0.165	0.003	–0.002	–0.014
20.0	–0.104	–0.097	–0.090	–0.098	–0.007	–0.007	0.008
King $c = 30$ , FWHM = 1.0 pixels							
3.0	0.271	0.268	0.270	0.283	0.003	–0.002	–0.013
20.0	–0.226	–0.219	–0.213	–0.222	–0.007	–0.006	0.009
MOFFAT15, FWHM = 0.5 pixels							
3.0	0.123	0.119	0.121	0.135	0.004	–0.002	–0.014
20.0	–0.137	–0.130	–0.123	–0.130	–0.007	–0.007	0.007
MOFFAT15, FWHM = 1.0 pixels							
3.0	0.191	0.187	0.191	0.203	0.004	–0.004	–0.012
20.0	–0.194	–0.187	–0.180	–0.189	–0.007	–0.007	0.009

Table 3. Comparison of ground-based and HST data for clusters in NGC 6946. No corrections for reddening have been applied. Effective radii ( $R_e$ ) are in pc.

ID (L99)	Ground					HST					
	$V$	$U-B$	$B-V$	$V-I$	$R_e$	$V$	$V_{15}$	$U-B$	$B-V$	$V-I$	$R_e$
1258	19.50	0.02	0.61	1.00	5.9	$19.77 \pm 0.01$	$19.46 \pm 0.01$	$0.05 \pm 0.03$	$0.58 \pm 0.01$	$1.05 \pm 0.01$	4.9
1371	21.07	0.11	0.66	0.91	6.6	$21.61 \pm 0.03$	-	$0.14 \pm 0.21$	$0.63 \pm 0.06$	$0.90 \pm 0.04$	0.9
1561	19.49	-0.49	0.38	0.75	7.2	$19.84 \pm 0.01$	$19.49 \pm 0.02$	$-0.51 \pm 0.02$	$0.42 \pm 0.01$	$0.71 \pm 0.01$	1.5
2064	19.94	-0.63	0.26	0.54	6.5	$20.27 \pm 0.01$	$19.88 \pm 0.02$	$-0.61 \pm 0.02$	$0.26 \pm 0.02$	$0.52 \pm 0.02$	2.0
2074	21.07	-0.08	0.45	0.89	6.9	$21.27 \pm 0.02$	$20.98 \pm 0.05$	$-0.20 \pm 0.09$	$0.60 \pm 0.04$	$0.97 \pm 0.02$	4.0
2075	20.48	-0.02	0.71	1.26	9.9	$20.84 \pm 0.02$	$20.52 \pm 0.04$	$0.20 \pm 0.14$	$0.84 \pm 0.04$	$1.42 \pm 0.02$	1.7
2350	18.52	-0.58	0.35	0.63	8.9	$19.17 \pm 0.01$	$18.29 \pm 0.02$	$-0.61 \pm 0.03$	$0.29 \pm 0.02$	$0.63 \pm 0.03$	0.5
2811	21.27	0.00	0.45	1.07	14.5	$21.65 \pm 0.03$	$21.51 \pm 0.09$	$-0.17 \pm 0.11$	$0.47 \pm 0.05$	$1.05 \pm 0.03$	1.8
2845	21.07	0.06	0.38	0.90	12.6	$21.51 \pm 0.02$	$21.37 \pm 0.07$	$0.02 \pm 0.12$	$0.43 \pm 0.04$	$0.87 \pm 0.03$	2.9
2956	20.77	-0.07	0.39	0.92	6.4	$20.95 \pm 0.01$	$20.67 \pm 0.04$	$-0.05 \pm 0.07$	$0.43 \pm 0.03$	$0.91 \pm 0.02$	3.7

Table 4. Cluster candidates in field NGC 6946–3 selected from HST images. No correction for reddening has been applied to the photometry in the table.

chip/ID	x	y	$V$	$U-B$	$B-V$	$V-I$	FWHM pixels	log(age) years	Mass $10^3 M_{\odot}$
WF2/50	395	81	$22.19 \pm 0.03$	$0.04 \pm 0.17$	$0.54 \pm 0.06$	$0.95 \pm 0.04$	0.40	$8.00 \pm 0.29$	$22 \pm 11$
WF2/63	321	93	$22.38 \pm 0.03$	$-0.70 \pm 0.08$	$0.35 \pm 0.07$	$0.25 \pm 0.06$	0.62	< 7.0	$3 \pm 2$
WF2/113	464	147	$22.32 \pm 0.03$	$-0.30 \pm 0.12$	$0.45 \pm 0.06$	$0.86 \pm 0.04$	0.54	$7.50 \pm 0.26$	$10 \pm 4$
WF2/172	200	226	$22.25 \pm 0.03$	$-0.08 \pm 0.14$	$0.48 \pm 0.06$	$1.01 \pm 0.04$	0.46	$7.85 \pm 0.25$	$17 \pm 7$
WF2/211	70	317	$22.24 \pm 0.03$	$-0.22 \pm 0.12$	$0.43 \pm 0.06$	$1.00 \pm 0.04$	0.41	$7.66 \pm 0.22$	$14 \pm 5$
WF2/226	430	340	$19.85 \pm 0.01$	$-0.07 \pm 0.03$	$0.57 \pm 0.01$	$0.98 \pm 0.01$	1.52	$7.80 \pm 0.14$	$153 \pm 36$
WF2/233	622	344	$22.32 \pm 0.03$	$-0.77 \pm 0.09$	$0.37 \pm 0.07$	$0.39 \pm 0.06$	0.40	< 7.0	$3 \pm 3$
WF2/262	254	383	$21.94 \pm 0.02$	$-0.15 \pm 0.11$	$0.62 \pm 0.05$	$0.94 \pm 0.03$	0.55	$7.63 \pm 0.21$	$18 \pm 6$
WF2/263	653	383	$22.21 \pm 0.03$	$-0.47 \pm 0.10$	$0.54 \pm 0.06$	$1.20 \pm 0.04$	0.24	$7.08 \pm 0.30$	$5 \pm 2$
WF2/278	549	415	$22.45 \pm 0.04$	$-0.60 \pm 0.10$	$0.20 \pm 0.08$	$0.76 \pm 0.06$	5.47	$7.14 \pm 0.27$	$4 \pm 2$
WF2/299	221	449	$22.40 \pm 0.03$	$-0.26 \pm 0.12$	$0.43 \pm 0.06$	$0.98 \pm 0.04$	0.32	$7.59 \pm 0.23$	$11 \pm 4$
WF2/338	279	512	$20.34 \pm 0.01$	$-0.23 \pm 0.03$	$0.39 \pm 0.02$	$0.81 \pm 0.01$	1.01	$7.67 \pm 0.14$	$82 \pm 19$
WF2/357	700	530	$21.86 \pm 0.02$	$0.21 \pm 0.20$	$0.55 \pm 0.05$	$0.84 \pm 0.03$	1.77	$8.34 \pm 0.46$	$49 \pm 39$
WF2/379	359	544	$22.21 \pm 0.03$	$-0.40 \pm 0.09$	$0.40 \pm 0.06$	$1.15 \pm 0.04$	0.78	$7.36 \pm 0.21$	$9 \pm 3$
WF2/398	144	564	$22.06 \pm 0.03$	$0.06 \pm 0.14$	$0.41 \pm 0.05$	$0.96 \pm 0.03$	0.77	$8.15 \pm 0.29$	$31 \pm 15$
WF2/469	625	645	$21.63 \pm 0.02$	$-0.72 \pm 0.09$	$0.76 \pm 0.07$	$0.72 \pm 0.04$	0.48	< 7.0	$7 \pm 1$
WF2/470	626	647	$21.58 \pm 0.02$	$-0.73 \pm 0.05$	$0.37 \pm 0.04$	$0.65 \pm 0.03$	0.48	< 7.0	$7 \pm 3$
WF2/503	77	673	$19.73 \pm 0.01$	$-0.20 \pm 0.02$	$0.38 \pm 0.01$	$0.81 \pm 0.01$	0.94	$7.72 \pm 0.14$	$154 \pm 36$
WF2/544	742	705	$22.31 \pm 0.04$	$-0.70 \pm 0.07$	$0.22 \pm 0.06$	$0.47 \pm 0.05$	0.34	< 7.0	$3 \pm 1$
WF2/554	718	713	$22.13 \pm 0.03$	$-0.71 \pm 0.09$	$0.42 \pm 0.07$	$1.49 \pm 0.04$	0.35	< 7.0	$4 \pm 3$
WF2/589	431	744	$22.04 \pm 0.03$	$-0.31 \pm 0.09$	$0.48 \pm 0.05$	$1.21 \pm 0.03$	0.23	$7.47 \pm 0.19$	$13 \pm 4$
WF3/47	130	108	$22.46 \pm 0.04$	$-0.10 \pm 0.24$	$0.65 \pm 0.10$	$0.92 \pm 0.05$	2.61	$7.69 \pm 0.38$	$12 \pm 7$
WF3/82	130	166	$21.40 \pm 0.02$	$-0.13 \pm 0.08$	$0.56 \pm 0.04$	$0.99 \pm 0.02$	1.20	$7.70 \pm 0.20$	$32 \pm 11$
WF3/104	604	185	$22.27 \pm 0.03$	$-0.65 \pm 0.08$	$0.32 \pm 0.06$	$0.75 \pm 0.05$	0.32	< 7.0	$4 \pm 2$
WF3/123	614	206	$21.64 \pm 0.02$	$0.05 \pm 0.11$	$0.41 \pm 0.04$	$0.89 \pm 0.03$	0.79	$8.13 \pm 0.28$	$44 \pm 21$
WF3/128	546	216	$21.95 \pm 0.03$	$-0.07 \pm 0.13$	$0.46 \pm 0.06$	$0.98 \pm 0.04$	0.37	$7.88 \pm 0.24$	$24 \pm 9$
WF3/130	547	221	$21.28 \pm 0.02$	$-0.21 \pm 0.06$	$0.47 \pm 0.03$	$0.83 \pm 0.02$	0.66	$7.64 \pm 0.16$	$33 \pm 9$
WF3/137	512	227	$21.92 \pm 0.03$	$0.04 \pm 0.25$	$1.19 \pm 0.08$	$1.62 \pm 0.03$	0.25	$7.50 \pm 0.48$	$15 \pm 12$
WF3/151	570	244	$22.22 \pm 0.03$	$-0.31 \pm 0.10$	$0.38 \pm 0.06$	$0.80 \pm 0.04$	0.60	$7.54 \pm 0.23$	$12 \pm 4$
WF3/190	522	286	$21.43 \pm 0.02$	$-0.09 \pm 0.07$	$0.36 \pm 0.03$	$0.89 \pm 0.02$	0.70	$7.92 \pm 0.17$	$41 \pm 11$
WF3/239	515	332	$21.46 \pm 0.02$	$-0.17 \pm 0.08$	$0.55 \pm 0.04$	$1.04 \pm 0.03$	0.86	$7.65 \pm 0.18$	$28 \pm 8$
WF3/245	512	338	$22.33 \pm 0.04$	$-0.26 \pm 0.15$	$0.56 \pm 0.08$	$1.15 \pm 0.05$	0.41	$7.49 \pm 0.26$	$10 \pm 4$
WF3/250	496	347	$21.66 \pm 0.02$	$-0.23 \pm 0.07$	$0.49 \pm 0.04$	$1.10 \pm 0.03$	0.47	$7.59 \pm 0.18$	$22 \pm 7$
WF3/272	790	361	$22.43 \pm 0.05$	$-0.33 \pm 0.17$	$0.59 \pm 0.10$	$0.95 \pm 0.06$	0.93	$7.33 \pm 0.35$	$7 \pm 4$
WF3/286	89	374	$21.02 \pm 0.01$	$-0.64 \pm 0.04$	$0.30 \pm 0.03$	$0.49 \pm 0.03$	0.22	< 7.0	$13 \pm 3$
WF3/321	451	400	$21.98 \pm 0.03$	$-0.06 \pm 0.16$	$0.67 \pm 0.06$	$1.07 \pm 0.04$	0.32	$7.74 \pm 0.27$	$19 \pm 9$
WF3/344	667	417	$21.32 \pm 0.02$	$-0.19 \pm 0.06$	$0.47 \pm 0.03$	$0.91 \pm 0.02$	0.27	$7.67 \pm 0.17$	$33 \pm 9$
WF3/416	71	469	$21.18 \pm 0.01$	$-0.36 \pm 0.04$	$0.36 \pm 0.03$	$0.93 \pm 0.02$	0.29	$7.47 \pm 0.15$	$29 \pm 7$
WF3/425	438	481	$21.81 \pm 0.03$	$-0.29 \pm 0.09$	$0.63 \pm 0.05$	$1.04 \pm 0.03$	0.58	$7.37 \pm 0.21$	$13 \pm 5$
WF3/486	293	523	$21.41 \pm 0.02$	$-0.29 \pm 0.06$	$0.44 \pm 0.03$	$0.97 \pm 0.02$	0.35	$7.53 \pm 0.16$	$25 \pm 7$
WF3/488	428	524	$22.41 \pm 0.04$	$0.03 \pm 0.21$	$0.51 \pm 0.08$	$0.90 \pm 0.05$	0.62	$8.01 \pm 0.35$	$18 \pm 11$

Table 4—Continued

chip/ID	x	y	$V$	$U-B$	$B-V$	$V-I$	FWHM pixels	log(age) years	Mass $10^3 M_{\odot}$
WF3/497	308	533	$21.90 \pm 0.03$	$-0.08 \pm 0.13$	$0.68 \pm 0.05$	$1.30 \pm 0.03$	0.49	$7.69 \pm 0.27$	$20 \pm 9$
WF3/502	152	536	$21.49 \pm 0.02$	$0.68 \pm 0.43$	$1.18 \pm 0.06$	$1.72 \pm 0.02$	0.62	$8.95 \pm 0.51$	$206 \pm 180$
WF3/553	694	566	$22.45 \pm 0.04$	$-0.23 \pm 0.17$	$0.59 \pm 0.09$	$1.19 \pm 0.05$	0.44	$7.51 \pm 0.34$	$9 \pm 5$
WF3/612	423	598	$21.04 \pm 0.01$	$-0.06 \pm 0.06$	$0.45 \pm 0.03$	$0.87 \pm 0.02$	1.08	$7.90 \pm 0.17$	$57 \pm 17$
WF3/613	55	599	$21.69 \pm 0.03$	$-0.52 \pm 0.06$	$0.42 \pm 0.05$	$0.92 \pm 0.03$	0.32	$7.09 \pm 0.19$	$8 \pm 2$
WF3/620	133	605	$21.99 \pm 0.04$	$-0.76 \pm 0.07$	$0.24 \pm 0.07$	$0.50 \pm 0.07$	0.47	$< 7.0$	$5 \pm 3$
WF3/630	133	609	$22.16 \pm 0.04$	$-0.78 \pm 0.09$	$0.34 \pm 0.09$	$0.71 \pm 0.07$	0.22	$< 7.0$	$4 \pm 3$
WF3/737	273	664	$22.00 \pm 0.03$	$-0.41 \pm 0.10$	$0.77 \pm 0.07$	$1.07 \pm 0.04$	0.21	$< 7.0$	$5 \pm 2$
WF3/742	637	665	$22.43 \pm 0.04$	$-0.24 \pm 0.13$	$0.39 \pm 0.07$	$0.74 \pm 0.05$	0.37	$7.65 \pm 0.28$	$11 \pm 5$
WF3/748	326	666	$20.30 \pm 0.01$	$-0.75 \pm 0.02$	$0.32 \pm 0.02$	$0.54 \pm 0.01$	0.73	$< 7.0$	$25 \pm 6$
WF3/754	202	669	$21.56 \pm 0.02$	$0.03 \pm 0.12$	$0.55 \pm 0.05$	$1.08 \pm 0.03$	1.61	$7.97 \pm 0.26$	$39 \pm 17$
WF3/802	674	696	$22.33 \pm 0.04$	$0.04 \pm 0.20$	$0.38 \pm 0.07$	$0.84 \pm 0.05$	1.25	$8.13 \pm 0.46$	$23 \pm 18$
WF3/928	90	785	$22.33 \pm 0.04$	$-0.36 \pm 0.11$	$0.34 \pm 0.06$	$1.27 \pm 0.04$	0.58	$7.49 \pm 0.24$	$10 \pm 4$
WF3/930	410	785	$21.61 \pm 0.02$	$-0.38 \pm 0.06$	$0.38 \pm 0.04$	$0.84 \pm 0.03$	0.21	$7.42 \pm 0.18$	$18 \pm 5$
WF3/931	756	785	$22.25 \pm 0.09$	$-0.22 \pm 0.16$	$0.56 \pm 0.11$	$0.80 \pm 0.09$	0.86	$7.55 \pm 0.33$	$12 \pm 6$
WF4/19	275	64	$19.85 \pm 0.01$	$-0.43 \pm 0.02$	$0.55 \pm 0.01$	$0.72 \pm 0.01$	0.29	$7.17 \pm 0.14$	$56 \pm 13$
WF4/36	637	77	$21.16 \pm 0.03$	$-0.59 \pm 0.06$	$0.42 \pm 0.05$	$0.60 \pm 0.04$	0.49	$< 7.0$	$11 \pm 4$
WF4/38	636	78	$21.20 \pm 0.02$	$-0.59 \pm 0.06$	$0.44 \pm 0.05$	$0.70 \pm 0.04$	0.49	$< 7.0$	$11 \pm 4$
WF4/150	793	162	$22.42 \pm 0.07$	$-0.23 \pm 0.19$	$0.37 \pm 0.11$	$0.87 \pm 0.10$	2.20	$7.69 \pm 0.32$	$12 \pm 6$
WF4/178	462	181	$21.52 \pm 0.02$	$-0.39 \pm 0.05$	$0.30 \pm 0.03$	$0.65 \pm 0.03$	0.36	$7.47 \pm 0.16$	$21 \pm 5$
WF4/233	576	225	$20.66 \pm 0.01$	$-0.23 \pm 0.03$	$0.42 \pm 0.02$	$0.87 \pm 0.01$	0.74	$7.65 \pm 0.14$	$60 \pm 14$
WF4/264	527	246	$22.46 \pm 0.04$	$0.21 \pm 0.28$	$0.59 \pm 0.08$	$1.00 \pm 0.05$	0.58	$8.29 \pm 0.64$	$26 \pm 28$
WF4/280	186	259	$22.31 \pm 0.04$	$0.39 \pm 0.31$	$0.53 \pm 0.07$	$0.94 \pm 0.05$	0.82	$8.55 \pm 0.26$	$45 \pm 20$
WF4/296	641	269	$20.39 \pm 0.01$	$-0.58 \pm 0.02$	$0.25 \pm 0.02$	$0.46 \pm 0.02$	0.62	$7.14 \pm 0.14$	$31 \pm 7$
WF4/301	713	272	$21.13 \pm 0.02$	$-0.03 \pm 0.06$	$0.41 \pm 0.03$	$0.77 \pm 0.03$	0.71	$7.98 \pm 0.17$	$58 \pm 17$
WF4/332	350	294	$21.92 \pm 0.03$	$-0.55 \pm 0.14$	$1.08 \pm 0.09$	$1.39 \pm 0.04$	1.70	$< 7.0$	$5 \pm 1$
WF4/371	759	318	$22.04 \pm 0.03$	$-0.29 \pm 0.11$	$0.47 \pm 0.06$	$1.10 \pm 0.04$	1.16	$7.50 \pm 0.24$	$13 \pm 5$
WF4/373	734	322	$20.95 \pm 0.01$	$0.20 \pm 0.11$	$0.87 \pm 0.03$	$1.49 \pm 0.02$	0.42	$8.02 \pm 0.21$	$73 \pm 26$
WF4/460	769	394	$22.24 \pm 0.04$	$-0.17 \pm 0.14$	$0.34 \pm 0.08$	$0.90 \pm 0.06$	2.65	$7.80 \pm 0.25$	$16 \pm 7$
WF4/497	790	423	$21.90 \pm 0.03$	$-0.25 \pm 0.11$	$0.57 \pm 0.06$	$1.12 \pm 0.04$	0.99	$7.50 \pm 0.24$	$15 \pm 6$
WF4/530	659	445	$22.28 \pm 0.03$	$0.30 \pm 0.45$	$1.06 \pm 0.10$	$1.61 \pm 0.04$	0.62	$9.89 \pm 0.13$	$706 \pm 158$
WF4/551	249	463	$22.41 \pm 0.04$	$-0.60 \pm 0.14$	$0.69 \pm 0.10$	$1.06 \pm 0.06$	0.77	$< 7.0$	$3 \pm 4$
WF4/554	619	468	$22.10 \pm 0.03$	$0.26 \pm 0.20$	$0.44 \pm 0.06$	$0.92 \pm 0.04$	0.95	$8.48 \pm 0.20$	$49 \pm 16$
WF4/606	260	500	$21.45 \pm 0.02$	$-0.60 \pm 0.06$	$0.47 \pm 0.04$	$0.68 \pm 0.03$	0.41	$< 7.0$	$8 \pm 3$
WF4/614	262	505	$22.05 \pm 0.04$	$-0.53 \pm 0.10$	$0.47 \pm 0.07$	$0.64 \pm 0.06$	0.41	$7.00 \pm 0.30$	$5 \pm 2$
WF4/657	137	536	$19.88 \pm 0.01$	$0.07 \pm 0.03$	$0.60 \pm 0.01$	$1.05 \pm 0.01$	1.24	$8.00 \pm 0.14$	$191 \pm 46$
WF4/719	181	579	$22.38 \pm 0.04$	$-0.66 \pm 0.08$	$0.22 \pm 0.07$	$0.45 \pm 0.06$	0.98	$< 7.0$	$3 \pm 1$
WF4/747	624	600	$22.41 \pm 0.04$	$-0.73 \pm 0.12$	$0.66 \pm 0.10$	$1.88 \pm 0.05$	0.55	$< 7.0$	$3 \pm 0$
WF4/755	63	609	$21.64 \pm 0.02$	$0.02 \pm 0.21$	$0.94 \pm 0.07$	$1.29 \pm 0.03$	2.47	$7.66 \pm 0.34$	$24 \pm 14$
WF4/758	222	611	$21.80 \pm 0.03$	$-0.57 \pm 0.06$	$0.33 \pm 0.05$	$0.72 \pm 0.04$	0.50	$7.07 \pm 0.21$	$7 \pm 2$
WF4/791	588	641	$21.27 \pm 0.02$	$0.45 \pm 0.38$	$1.37 \pm 0.06$	$1.86 \pm 0.02$	0.83	$9.89 \pm 6.97$	$1790 \pm 21478$



Table 4—Continued

chip/ID	x	y	$V$	$U-B$	$B-V$	$V-I$	FWHM pixels	log(age) years	Mass $10^3 M_\odot$
WF4/822	409	672	$22.42 \pm 0.04$	$-0.04 \pm 0.18$	$0.41 \pm 0.08$	$0.94 \pm 0.05$	0.31	$7.96 \pm 0.36$	$17 \pm 10$
WF4/824	398	674	$22.20 \pm 0.04$	$-0.21 \pm 0.13$	$0.57 \pm 0.07$	$1.05 \pm 0.04$	0.30	$7.56 \pm 0.28$	$12 \pm 6$
WF4/849	369	694	$21.62 \pm 0.02$	$-0.37 \pm 0.08$	$0.49 \pm 0.05$	$0.98 \pm 0.03$	2.77	$7.34 \pm 0.20$	$15 \pm 5$
WF4/851	417	695	$22.12 \pm 0.03$	$-0.25 \pm 0.10$	$0.42 \pm 0.06$	$0.90 \pm 0.04$	0.58	$7.61 \pm 0.23$	$14 \pm 5$
WF4/895	768	757	$19.93 \pm 0.01$	$-0.50 \pm 0.02$	$0.41 \pm 0.01$	$0.71 \pm 0.01$	0.45	$7.15 \pm 0.14$	$49 \pm 11$
WF4/905	779	765	$22.35 \pm 0.06$	$-0.52 \pm 0.15$	$0.57 \pm 0.11$	$0.71 \pm 0.08$	0.51	$< 7.0$	$3 \pm 3$
WF4/908	792	769	$22.09 \pm 0.06$	$-0.64 \pm 0.12$	$0.41 \pm 0.10$	$0.50 \pm 0.10$	0.98	$< 7.0$	$4 \pm 3$
WF4/926	392	784	$22.41 \pm 0.04$	$-0.09 \pm 0.16$	$0.28 \pm 0.07$	$0.80 \pm 0.05$	1.00	$7.98 \pm 0.32$	$18 \pm 10$

Table 5. Luminosity function fits to cluster candidates.  $N$  is the number of clusters fitted. the column labeled  $\alpha$  gives the exponent for fits of the form  $dN(L)/dL = \beta L^\alpha$  while  $a$  and  $b$  refer to fits of the form  $\log \Sigma_{\text{cl}}[\text{kpc}^{-2}] = b + aM_V$ . The last column lists  $c = \beta/\Sigma_{\text{SFR}}$  for  $\alpha = -2.4$ . Milky

Way numbers in paranthesis are based on an assumed LF with  $\alpha = -2.4$ , normalized to the observed cluster density near the Sun at  $M_V = -8$ .

Galaxy (1)	Fit interval (2)	$N$ (3)	$b$ (4)	$a$ (5)	$\alpha$ (6)	$\Sigma_{\text{cl}}^{-8}$ (7)	$c$ (8)
NGC628	$-10.00 < M_V < -7.75$	60	$3.96 \pm 0.95$	$0.46 \pm 0.11$	$-2.16 \pm 0.26$	1.8	$7.96 \times 10^{-6}$
NGC1313	$-8.00 < M_V < -6.00$	259	$3.70 \pm 0.35$	$0.40 \pm 0.05$	$-2.01 \pm 0.12$	2.9	$5.94 \times 10^{-6}$
NGC1313	$-9.00 < M_V < -7.50$	52	$5.27 \pm 1.58$	$0.60 \pm 0.19$	$-2.51 \pm 0.47$	2.7	$5.58 \times 10^{-6}$
NGC3184	$-9.50 < M_V < -7.00$	72	$4.56 \pm 0.88$	$0.57 \pm 0.11$	$-2.42 \pm 0.26$	1.0	$4.80 \times 10^{-6}$
NGC5236	$-8.00 < M_V < -6.00$	228	$4.70 \pm 0.34$	$0.50 \pm 0.05$	$-2.25 \pm 0.12$	5.1	$3.03 \times 10^{-6}$
NGC5236	$-9.00 < M_V < -7.50$	34	$5.23 \pm 2.24$	$0.58 \pm 0.27$	$-2.44 \pm 0.67$	4.2	$2.52 \times 10^{-6}$
NGC6744	$-9.00 < M_V < -6.00$	60	$3.55 \pm 0.36$	$0.46 \pm 0.05$	$-2.14 \pm 0.12$	0.8	$1.05 \times 10^{-5}$
NGC6946	$-10.75 < M_V < -8.00$	243	$5.46 \pm 0.45$	$0.57 \pm 0.05$	$-2.42 \pm 0.12$	8.1	$1.45 \times 10^{-5}$
LMC	$-9.50 < M_V < -6.00$	251	$3.56 \pm 0.26$	$0.40 \pm 0.03$	$-2.01 \pm 0.08$	2.2	$1.21 \times 10^{-5}$
Milky Way	-	-	(4.43)	(0.56)	(-2.4)	0.89	-

Table 6. Galaxies from LR2000 and BHE02. Galaxies marked with an asterisk ( $\star$ ) are those studied in detail in the present paper.

Galaxy	$\Sigma_{\text{SFR}}$ $10^{-3} M_{\odot} \text{ kpc}^{-2} \text{ yr}^{-1}$	$A$ $\text{kpc}^2$	$M_V^{\text{max}}$ (obs)
From LR2000			
NGC45	0.23	110	−8.8
NGC247	0.18	200	−10.2
NGC300	0.49	159	−9.9
NGC628 $\star$	1.88	527	−11.3
NGC1156	3.07	60	−11.1
NGC1313 $\star$	4.04	105	−12.1
NGC2403	0.97	348	−9.9
NGC2835	0.73	126	−10.9
NGC2997	3.07	606	−12.9
NGC3184 $\star$	1.72	230	−10.6
NGC3621	1.67	527	−11.9
NGC4395	0.25	200	−9.1
NGC5204	0.83	38	−9.6
NGC5236 $\star$	13.76	166	−11.7
NGC5585	0.32	105	−10.8
NGC6744 $\star$	0.62	695	−11.0
NGC6946 $\star$	4.60	552	−13.0
NGC7424	0.18	960	−11.4
NGC7793	2.12	66	−10.4
LR2000, litt. data			
NGC1569	9.43	13	−13.9
NGC1705	2.16	6	−13.7
NGC1741	12.78	382	−15.0
NGC5253	7.29	29	−11.1
IC1613	0.05	9	−5.8
LMC	1.52	79	−10.0
From BHE02			
NGC4214	3.80	21	−12.04
NGC2366	1.95	19	−9.51
DDO50	1.26	8.6	−7.91

Table 6—Continued

Galaxy	$\Sigma_{\text{SFR}}$ $10^{-3} \text{ M}_{\odot} \text{ kpc}^{-2} \text{ yr}^{-1}$	$A$ $\text{kpc}^2$	$M_V^{\text{max}}$ (obs)
DDO168	0.85	5.1	−7.58
DDO165	0.18	3.0	−8.34
SexA	2.29	1.6	−7.12
Lick data			
NGC3521	3.58	382	−11.5
NGC4258	0.702	1414	−12.6
NGC5055	2.98	504	−11.4
NGC5194	8.21	578	−12.8
IC2574	0.17	121	−10.5

This figure "Larsen.fig1a.jpg" is available in "jpg" format from:

<http://arxiv.org/ps/astro-ph/0206295v1>

This figure "Larsen.fig1b.jpg" is available in "jpg" format from:

<http://arxiv.org/ps/astro-ph/0206295v1>

This figure "Larsen.fig1c.jpg" is available in "jpg" format from:

<http://arxiv.org/ps/astro-ph/0206295v1>

This figure "Larsen.fig1d.jpg" is available in "jpg" format from:

<http://arxiv.org/ps/astro-ph/0206295v1>

This figure "Larsen.figure.jpg" is available in "jpg" format from:

<http://arxiv.org/ps/astro-ph/0206295v1>



This figure "Larsen.fig1f.jpg" is available in "jpg" format from:

<http://arxiv.org/ps/astro-ph/0206295v1>